Monthly Notices of the ROYAL ASTRONOMICAL SOCIETY

MNRAS **544,** 3361–3378 (2025) https://doi.org/10.1093/mnras/staf1887
Advance Access publication 2025 October 31

Shock-driven heating in the circumnuclear star-forming regions of NGC 7582: insights from *JWST* NIRSpec and MIRI/MRS spectroscopy

Oscar Veenema [1]★ Niranjan Thatte [1] Dimitra Rigopoulou [1,2] Ismael García-Bernete,[3] Almudena Alonso-Herrero,[3] Anelise Audibert,[4,5] Enrica Bellocchi,[6] Andrew J. Bunker,[1] Steph Campbell [7] Francoise Combes,[8] Ric I. Davies [9] Daniel Delaney,[10,11] Fergus Donnan [1] Federico Esposito,[12] Santiago García-Burillo,[12] Omaira Gonzalez Martin [13] Laura Hermosa Muñoz [3] Erin K. S. Hicks,[10,11,14] Sebastian F. Hoenig,[15] Nancy A. Levenson,[16] Chris Packham,[14,17] Miguel Pereira-Santaella,[18] Cristina Ramos Almeida [4,5] Claudio Ricci,[19,20] Rogemar A. Riffel [21,22] David Rosario[7] and Lulu Zhang [14]

Affiliations are listed at the end of the paper

Accepted 2025 October 29. Received 2025 October 28; in original form 2025 June 13

ABSTRACT

We present combined *James Webb Space Telescope* (*JWST*) NIRSpec and MIRI/MRS integral field spectroscopy data of the nuclear and circumnuclear regions of the highly dust obscured Seyfert 2 galaxy NGC 7582, which is part of the sample of active galactic nucleaus (AGN) in the Galaxy Activity, Torus and Outflow Survey (GATOS). Spatially resolved analysis of the pure rotational H_2 lines (S(1)–S(7)) reveals a characteristic power-law temperature distribution in different apertures, with the two prominent southern star-forming regions exhibiting unexpectedly high molecular gas temperatures, comparable to those in the AGN powered nuclear region. We investigate potential heating mechanisms including direct AGN photoionization, UV fluorescent excitation from young star clusters, and shock excitation. We find that shock heating gives the most plausible explanation, consistent with multiple near- and mid-IR tracers and diagnostics. Using photoionization models from the PhotoDissociation Region Toolbox, we quantify the ISM conditions in the different regions, determining that the southern star-forming regions have a high density ($n_{\rm H} \sim 10^5$ cm^{-3}) and are irradiated by a moderate UV radiation field ($G_0 \sim 10^3$ Habing). Fitting a suite of Paris-Durham shock models to the rotational H_2 lines, as well as rovibrational 1-0 S(1), 1-0 S(2), and 2-1 S(1) H_2 emission lines, we find that a slow ($v_s \sim 10$ km s^{-1}) C-type shock is likely responsible for the elevated temperatures. Our analysis loosely favours local starburst activity as the driver of the shocks and circumnuclear gas dynamics in NGC 7582, though the possibility of an AGN jet contribution cannot be excluded.

Key words: galaxies: active – galaxies: individual: NGC 7582 – galaxies: kinematics and dynamics – galaxies: nuclei – galaxies: Seyfert – infrared: galaxies.

1 INTRODUCTION

At the centres of many galaxies reside active galactic nuclei (AGNs), powered by supermassive black hole (SMBH) accretion. AGNs play a crucial role in galaxy evolution (R. S. Somerville & R. Davé 2015), influencing their host environments through a range of feedback mechanisms, including their gas outflows (forming ionization cones), powerful relativistic jets that can shock the interstellar medium (ISM), and radiation from their accretion discs to name just a few (A. C. Fabian 2012; C. Harrison 2017; C. M. Harrison & C. Ramos Almeida 2024). While the source of AGN emission is highly localized (on the scale of less than a parsec), AGN impact extends across the entire galaxy, affecting different regions in diverse ways, from quenching star formation to driving outflows that regulate gas dynamics (I. Martín-Navarro et al. 2021; J. M. Piotrowska et al. 2022).

One key tracer of the physical properties of the ISM is molecular hydrogen (H_2), being the most abundant molecule in galaxies (T. J. Fletcher et al. 2021). Because the H_2 molecule lacks a permanent electric dipole moment, it emits lines in the infrared and far-ultraviolet which arise from transitions between its rotational and vibrational energy levels. Each of these transitions is characterized by a distinct excitation temperature, making H_2 an invaluable diagnostic tool for probing the physical conditions of the molecular gas phase within galaxies. The pure rotational $\nu = 0$–0 transitions are particularly valuable as they trace molecular gas with temperatures ranging from cool to warm ($T \sim 100$–1000 K; H. Roussel et al. 2007), with emission lines in the mid-infrared ($\sim 3 < \lambda < 30\,\mu$m). Therefore, H_2 rotational lines serve as sensitive tracers of warm

★ E-mail: oscar.veenema@physics.ox.ac.uk

molecular gas ($\gtrsim 100$ K), which is abundant in photodissociation regions (PDRs; D. Hollenbach & A. Tielens 1997; K. F. Kaplan et al. 2021).

The analysis of H_2 emission lines has become an increasingly valuable tool for probing ISM conditions and excitation mechanisms, particularly over the past few decades with the advent of space-based telescopes. One early study was conducted by D. Rigopoulou et al. (2002) who employed *Infrared Space Observatory* (*ISO*; M. Kessler et al. 1996) observations to investigate rotational H_2 emission in a sample of starburst and Seyfert galaxies, using these data to estimate the mass of warm molecular gas and explore possible excitation mechanisms. Subsequent studies using the *Spitzer* Space Telescope (M. W. Werner et al. 2004) further advanced this field. S. J. Higdon et al. (2006) observed rotational H_2 emission in numerous ultraluminous infrared galaxies (ULIRGs), deriving the temperature and mass of their warm molecular gas and concluding that the emission was consistent with an origin in PDRs associated with star formation. Additionally, H. Roussel et al. (2007) utilized *Spitzer* data from many galaxies to compare H_2 rotational emission across different galaxy morphologies, helping to constrain the dominant excitation mechanisms in galaxies of varying types. Collectively, studies such as these have demonstrated the diagnostic power of rotational H_2 emission lines in unveiling the physical processes shaping the ISM.

Some of the H_2 rovibrational emission lines are accessible from the ground and thus have historically been the widely studied. They trace hot molecular gas at temperatures of $\gtrsim 1000$ K, serving as important diagnostics of shocks, UV fluorescence, and X-ray heating in star-forming regions and AGN environments (e.g. R. I. Davies et al. 2003; A. Rodriguez-Ardila et al. 2004; E. Hicks et al. 2009; L. Colina et al. 2015; R. A. Riffel et al. 2021). However, they probe only a small fraction of the total molecular gas reservoir, as most of the gas remains at much lower kinetic temperatures, even in AGN-dominated systems. In contrast, the pure rotational lines directly probe the dominant warm molecular phase and are more representative of the bulk of the warm gas, though they remain inaccessible from the ground due to atmospheric absorption.

The launch of the *James Webb Space Telescope* (*JWST*; J. P. Gardner et al. 2023; J. Rigby et al. 2023) has revolutionized the study of AGN and their host galaxies. With its unparalleled sensitivity, *JWST*'s NIRSpec (P. Jakobsen et al. 2022; T. Böker et al. 2023) and MIRI/MRS (M. Wells et al. 2015; I. Argyriou et al. 2023) instruments enable the spatially resolved spectroscopy of galaxies with unprecedented spatial and spectral resolution compared to other space missions. Thus, *JWST* observations allow for a detailed spatially resolved analysis of H_2 emission lines in nearby galaxies making it possible to quantify the influence of AGN with far greater precision than ever before.

M. Pereira-Santaella et al. (2022) analysed *JWST*/MIRI observations of rotational H_2 lines in the nuclear region of nearby galaxy NGC 7319, revealing that interactions between the AGN-driven jet and molecular gas in the galactic disc act to decelerate the jet, producing asymmetric radio hotspots. This provided valuable insights into the complex interplay between AGN outflows and the surrounding ISM through H_2 emission line analysis. Similarly, L. Armus et al. (2023) utilized MIRI observations of rotational H_2 lines to measure the warm molecular gas mass within the central 100 pc of the AGN in NGC 7469. Their analysis revealed a decelerating, stratified AGN driven outflow with broad, blueshifted high-ionization lines. This emphasized the remarkable capability of *JWST* to probe multiphase gas dynamics in AGN environments, advancing our understanding of the complex feedback mechanisms in such systems. Furthermore, R. Davies et al. (2024) used MIRI observations of rotational H_2 lines from and around the AGN in NGC 5728 to investigate the impact of shocks from its ionization cone on the surrounding ISM. By combining rovibrational and pure rotational H_2 lines, they identified moderate-velocity ($\sim 30\,\mathrm{km\,s^{-1}}$) shocks in dense gas ($n_\mathrm{H} \sim 10^5$ cm^{-3}) irradiated by an external UV field ($G_0 = 10^3$ Habing). This provided insights into the role of shock heating in shaping the molecular gas dynamics within AGN hosting galaxies. Moreover, D. Esparza-Arredondo et al. (2025) investigated warm H_2 emission in the active galaxy MCG−05 − 23−16 using *JWST*, in comparison with cold molecular gas traced by molecular CO emission lines from ALMA data. They found that the warmer H_2 exhibits significantly more complex kinematics than the cold component, highlighting the impact of AGN activity and localized star formation on the molecular gas near the nucleus. Collectively, studies such as these, and others (e.g. T. Bohn et al. 2024; J. Costa-Souza et al. 2024; C. Ramos Almeida et al. 2025), highlight the unique power of H_2 analyses with *JWST* in spatially resolving molecular gas properties and kinematics in AGN environments, shedding new light on how AGN driven processes influence the ISM.

The paper is structured as follows. Section 2 summarizes the properties of the target, NGC 7582. Section 3 describes the *JWST* NIRSpec and MIRI/MRS observations. In Section 4, we present results and the analysis of the emission lines, the kinematics and modelling of the H_2 line fluxes. We then present models to quantify the ISM parameters and fit shock models before contrasting our new results with previous work to assess the origin of shocks within NGC 7582. Finally, in Section 5 we present our conclusions.

2 NGC 7582

NGC 7582 is a nearby ($z \sim 0.00525$; V. Braito et al. 2017; $D \sim 22$ Mpc) inclined (M. Wold & E. Galliano 2006, $i = 58°$;) barred spiral galaxy that hosts a heavily dust-obscured, Compton-thick AGN, classified as a Seyfert 2 (S. Bianchi et al. 2009). The AGN is associated with strong radio emission and a well-defined ionization cone (S. Juneau et al. 2022), originally deduced through optical [O III] emission and comparison to a prominent H α-emitting, H II-rich disc (S. Morris et al. 1985). The central SMBH has been estimated to have a mass of $5.5 \times 10^7\,\mathrm{M}_\odot$ based on mid-IR [Ne II] emission line analysis (M. Wold et al. 2006). Of interest are the presence of a kinematically distinct core (KDC) in the innermost nuclear region (S. Juneau et al. 2022) associated with stars in a circumnuclear ring formed from gas in the disc with major axis ∼200 pc from the AGN (R. A. Riffel et al. 2009; A. Alonso-Herrero et al. 2020; S. García-Burillo et al. 2021), as well as a possible radio jet emanating almost perpendicular to the ionization cone (T. Ricci et al. 2018).

While the potential presence of a radio AGN jet is not the primary focus of this study, we will refer to it when we discuss the origin of the H_2 rotational lines. The primary evidence supporting the presence of the jet comes from extended radio emission (e.g. D. A. Forbes & R. Norris 1998), out to ~ 4 arcsec north and south of the AGN, but mostly concentrated out to ~ 2 arcsec. However, such knot-like radio structures can also arise from intense star formation. None the less, the nucleus of NGC 7582 is complex, harbouring an AGN, as well as a star-forming disc, see also J. Reunanen, M. Prieto & R. Siebenmorgen (2010), presenting an ideal subject for in-depth investigation into the impact of an AGN on its host galaxy. Additionally, NGC 7582 is

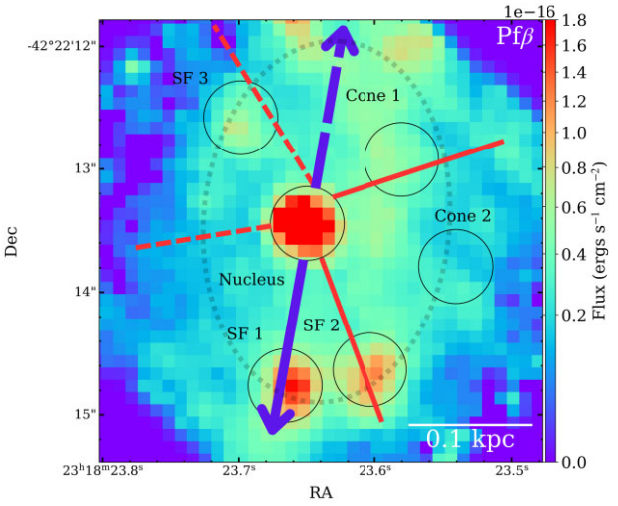

Figure 1. Pfβ (7–5) hydrogen recombination flux map from NIRSpec-IFS, highlighting regions of strong nuclear activity and/or star-formation. Circles denote apertures for which spectra were extracted. Red lines show the edges of the well established ionization cones (S. Morris et al. 1985). Dark blue arrows show the proposed direction of the bipolar jets from T. Ricci et al. (2018). Solid lines show orientation towards us and dashed show orientation away from us. The dotted black ellipse shows the approximate position of the star forming ring. North is up, East is to the left.

highly obscured along the line of sight to the nucleus with $A_V \sim 3.6$ mag (M. Ward et al. 1980).

Roughly 1 arcsec south of the nucleus, NGC 7582 hosts two prominent star-forming regions, previously identified and studied by M. Wold & E. Galliano (2006) and T. Ricci et al. (2018), where they were referred to as M1 and M2. These regions are highly luminous in hydrogen recombination lines. M. Wold & E. Galliano (2006) interpreted them as young star-forming clusters, estimating their ages to be approximately 1 Myr and suggesting that each may contain thousands of O-type stars. R. A. Riffel et al. (2009) further investigated these regions by comparing the equivalent widths (EWs) of their observed Brγ lines with those predicted by various evolutionary photoionization models. Following the methodology outlined in O. Dors et al. (2008), they estimated the clusters' ages to be ~ 5 Myr, with each potentially hosting around 500 O-type stars.

In Fig. 1 we present the hydrogen recombination Pfβ 4.654 μm line flux map of the nuclear region of NGC 7582, annotated to show the star-forming disc/ring, the edges of the ionization cones, and the putative AGN jet directions, based on their relative directions from the nucleus as presented in fig. 17 of T. Ricci et al. (2018). Aperture locations for key regions of interest are also indicated; spectra from these apertures form the basis of our analysis throughout this paper. Details of the observations, data reduction, and aperture extraction are provided in Section 3. Throughout this paper, all maps of NGC 7582 are shown with the same orientation where North is up and East to the left.

In our nomenclature, the two prominent southern star-forming regions, previously referred to as M1 and M2 (M. Wold & E. Galliano 2006; T. Ricci et al. 2018), are designated SF 1 and SF 2 to explicitly emphasize their star-forming nature. The selected apertures (Fig. 1) encompass key regions of interest within the nuclear region, providing a diverse sample for analysis. These include the central AGN-dominated region, the historically well-studied and luminous star-forming regions: SF 1 and SF 2, and two regions within the ionization cone: Cone 1, located at the northern edge, and Cone 2, a region within the cone itself. Additionally, an aperture is placed over SF 3, which, unlike SF 1 and SF 2, is not aligned with any potential jet and lies in front of the eastern ionization cone boundary. We give the relative RA and Dec of the centre of our apertures to the nucleus in the appendix, Table A1.

M. Wold & E. Galliano (2006) also identified three additional star-forming clusters in the northern circumnuclear ring, designated M3, M4, and M5. Although less luminous in hydrogen recombination line flux than the southern clusters (T. Ricci et al. 2018), they remain noteworthy. These northern clumps are excluded from our analysis due to limited spatial coverage in most MIRI/MRS observations. While not directly analysed, they are referenced throughout this study for comparison with the southern clusters.

The study by S. García-Burillo et al. (2021) used ALMA observations of NGC 7582 to probe the cold molecular gas via CO emission, indirectly tracing H_2 by assuming a CO-to-H_2 conversion factor. They identified a dusty, molecular-rich torus within ~ 10 pc of the AGN, a molecular gas deficit across the rest of the inner ~ 50 pc, and the molecular-rich star-forming ring at a radius of ~ 200 pc. They also traced an outflow originating within the ring, leading to the observed depletion of molecular gas in the central regions – a signature consistent with the presence of the ionization cone and AGN feedback. Moreover, our selected SF 1, SF 2, and SF 3 apertures all correspond to regions with strong 351 GHz continuum emission (top left panel of fig. 6 in S. García-Burillo et al. 2021), consistent with strong star formation.

3 OBSERVATIONS AND DATA REDUCTION

3.1 NIRSpec and MIRI/MRS data collection

The target studied here is part of the Galaxy Activity, Torus, and Outflow Survey (GATOS; A. Alonso-Herrero et al. 2021; S. García-Burillo et al. 2021; I. García-Bernete et al. 2024). The present study uses near-IR to mid-IR (2.87–28.1 μm) data collected with the integral-field spectrographs MIRI/MRS with a spectral resolution of R∼1300−3700 (A. Labiano et al. 2021), acquired on October 31st 2023, and NIRSpec with the grating-filter pairs G395H/F290LP (2.87–5.27 μm) with R∼2700 (T. Böker et al. 2022; P. Jakobsen et al. 2022), acquired on 7th April 2024. These data are part of the JWST Cycle 2 GO proposal ID 3535 (PI: I. García-Bernete and D. Rigopoulou).

For the NIRSpec observations, a 4-point medium-size cycling dither pattern optimized for extended sources was adopted, and the NRSRAPID readout mode with 3 groups per integration and 7 integrations per exposure was used. The same configuration was used for the dedicated LEAKCAL observations. For the MIRI/MRS observations, a 4-point extended-source dither pattern and the FASTR1 readout mode were used. Each exposure consisted of 65 groups per integration for the short (A) and medium (B) wavelength settings, and 121 groups per integration for the long (C) setting, with 1 integration per exposure. Background observations were obtained with the same readout settings but using a 2-point dither pattern. Note that for these particular observations, the MIRI/MRS guide star was missing leading to the wrong astrometry and incorrect absolute RA and Dec. coordinates (a pointing issue). We corrected these data cubes by shifting the coordinates so that the bright AGN position aligns with its RA and Dec. as seen with NIRSpec, where the astrometry was correct.

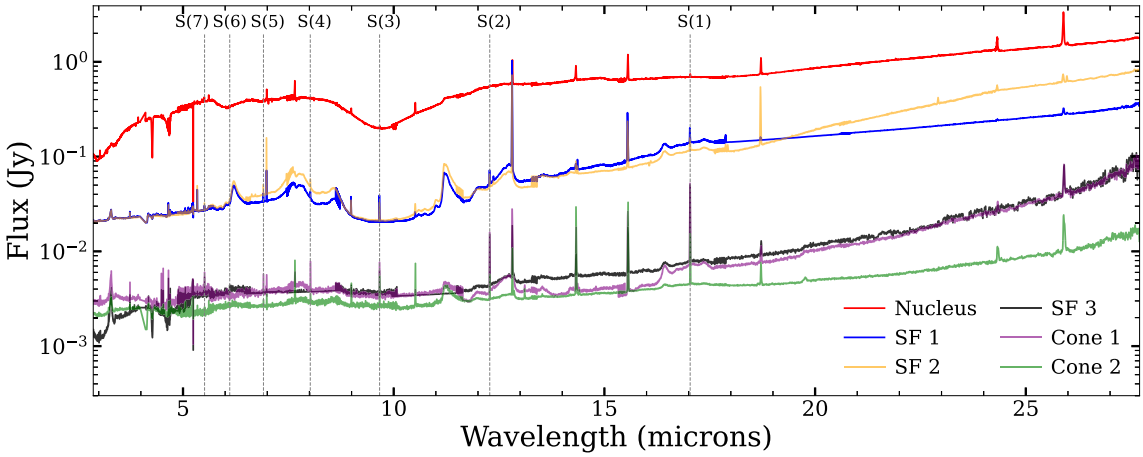

Figure 2. Observed spectrum (rest-frame) for each aperture after applying PSF corrections, but before any extinction corrections. Each line shows the total flux within each aperture at every wavelength bin available across the combined NIRSpec and MIRI/MRS wavelength range. Grey dotted lines show the locations of rotational H_2 lines S(1) to S(7). Many atomic emission lines are also clearly visible in each aperture but are not labelled for clarity.

3.2 NIRSpec and MIRI/MRS data reduction

For the data reduction, we primarily followed the standard pipeline procedure and the same configuration of the pipeline stages described in I. García-Bernete et al. (2022) and M. Pereira-Santaella et al. (2022) to reduce the data. Some hot and cold pixels are not identified by the current pipeline, so we added some extra steps as described in M. Pereira-Santaella et al. (2024) and I. García-Bernete et al. (2024) for NIRSpec and MIRI/MRS, respectively.

One dimensional spectra were extracted from apertures of radius 0.3 arcsec (corresponding to ∼30 pc in radius at the distance of NGC 7582). Their locations and designations are shown in Fig. 1, showing the hydrogen recombination Pfβ emission line from NIRSpec G395H/F290LP.

Aperture-specific point spread function (PSF) corrections were then applied to account for the impact of the PSF on the measured fluxes. The PSFs produced by *JWST* instruments for point sources are well characterized, and can be modeled using WebbPSF (M. D. Perrin et al. 2014). For the nuclear aperture, we applied the WebbPSF models directly for NIRSpec G395H/F290LP and MIRI/MRS. Since the nuclear emission is dominated by the AGN, which is effectively a point source, this provides a reliable correction. For the star-forming regions (SF 1, SF 2, and SF 3), the WebbPSF models were convolved with a Gaussian kernel of $\sigma = 0.1$ arcseconds to account for their spatially extended nature, For the remaining apertures (Cone 1 and Cone 2), the flux redistribution caused by the PSF is expected to balance out, as any flux loss from the aperture should be compensated by flux gained from surrounding spaxels therefore PSF corrections were not necessary for these apertures. Overall, these corrections were small, of order $\sim$ 10 per cent for each channel. The final spectra are presented in Fig. 2.

3.3 Extinction corrections

The nucleus of NGC 7582 is highly dust-extinguished, therefore, it is essential to account for the effects of extinction. Correcting for extragalactic dust extinction is a non-trivial task, with various approaches available (D. Calzetti 1996; M. Xue et al. 2016). In this work, we employ the differential extinction model developed by F. R. Donnan et al. (2024). We refer the reader to their paper for a detailed description of the model. In brief, the extinction within each aperture is modelled as a combination of multiple dust screens, each contributing differently to the total attenuation. The extinction of each screen is represented as $e^{-\tau_{9.8}\,\tau(\lambda)}$, where the parameter $\tau_{9.8}$ corresponds to the optical depth at 9.8 μm. The model assigns different weights to components with a range of optical depths and dust temperatures. Estimates of the extinction are provided through fitting various features such as the silicate absorption at 9.8 μm, the H_2 rotational S(3) line as well as the mid-infrared hydrogen recombination lines, allowing for a more physically motivated representation of the extinction compared to simpler screen or mixed models. As F. R. Donnan et al. (2024) show, the derived differential extinction model is versatile, and encompasses many different physical ISM conditions such as when the radiation source contains multiple contributions, as is the case here with the presence of an AGN and star-forming regions. The spectra from each aperture are fit using this model, and the resulting extinction correction factors are applied. We give our derived $\tau_{9.8}$ for each region in the appendix, Table A1. Extinction corrections have been applied to all line fluxes measured in our spectra.

3.4 Flux and kinematics maps

The velocity and velocity dispersion of each spectral line was determined by fitting Gaussian profiles to each continuum subtracted emission line using the CapFit routine (M. Cappellari 2023). The velocity, v, is calculated by comparing the centroid wavelength of the fitted Gaussian profile, λ, to the systemic wavelength of the line for the galaxy, λ_0. This is given by $v = c \times (\lambda - \lambda_0)/\lambda_0$, where c is the speed of light, and is valid for $v << c$, which is the case here. The velocity dispersion, σ_v, is similarly derived from the Gaussian fit parameters using: $\sigma_v = c \times \sigma/\lambda_0$, where σ is the best-fit Gaussian dispersion, expressed in the same units as λ_0.

Line flux, velocity, and velocity dispersion maps were produced following the steps outlined to individual spaxels for various emission lines within the NIRSpec and MIRI/MRS FOV of NGC 7582. To facilitate a direct comparison between different emission lines, all MIRI maps were reprojected (bilinear interpolation) to match the exact NIRSpec FOV using the `reproject_interp` function from T. Robitaille, C. Deil & A. Ginsburg (2020) – this was only done for creating maps, with all quantitative analysis being done using the original data cubes.

Table 1. Measured fluxes for the H_2 $\nu = 0$–0 S(1) to S(7) lines. Fluxes were corrected for extinction and are stated in units of 10^{-15} erg s^{-1} cm^{-2}. All apertures were circular with 0.3 arcsec radii.

Line	λ (μm)	Nucleus	SF 1	SF 2	SF 3	Cone 1	Cone 2
S(1)	17.035	12.8 ± 0.9	6.1 ± 0.1	8.10 ± 0.08	4.34 ± 0.02	2.941 ± 0.001	1.70 ± 0.01
S(2)	12.279	4.8 ± 1.4	4.01 ± 0.07	3.94 ± 0.05	1.60 ± 0.02	1.09 ± 0.02	0.52 ± 0.02
S(3)	9.665	32.5 ± 0.2	11.01 ± 0.02	12.42 ± 0.03	0.27 ± 0.03	2.83 ± 0.03	2.12 ± 0.02
S(4)	8.026	3.0 ± 1.3	1.2 ± 0.1	2.18 ± 0.09	0.06 ± 0.04	0.39 ± 0.03	0.08 ± 0.01
S(5)	6.909	7.4 ± 1.1	2.75 ± 0.02	3.80 ± 0.04	0.05 ± 0.01	0.29∗	0.13 ± 0.01
S(6)	6.109	4.4 ± 0.8	0.79 ± 0.03	0.90 ± 0.03	0.14 ± 0.04	0.10∗	0.57 ± 0.02
S(7)	5.512	-	1.3 ± 0.2	2.1 ± 0.1	0.32 ± 0.08	0.35∗	0.2 ± 0.1

∗: A small portion of Cone 1 lies slightly outside the MIRI/MRS FOV for these lines, leading to some flux not being measured, hence these fluxes are lower limits.

Table 2. Measured $\log_{10}$ emission line ratio values in each aperture. The [S III] line could not be fit in the SF 3 and Cone 2 apertures.

Region	[Ne III]/[Ne II]	[Ne V]/[Ne II]	[Ar II]/[Ar III]	[S IV]/[S III]	[Fe II]/Pfα
Nucleus	0.43	−0.21	−0.35	0.01	1.37∗
SF 1	−0.75	−1.84	−0.36	−0.32	1.32
SF 2	−0.34	−1.41	−0.62	−1.00	0.75
SF 3	−0.10	−0.57	−0.07	-	0.92∗
Cone 1	−0.19	−0.36	−0.44	−0.35	1.00∗
Cone 2	−0.57	−1.79	−0.72	-	1.14∗

∗: Pfαis poorly detected (low S/N) in these apertures, and so its flux is roughly inferred from Pfβassuming Case B recombination is valid, $T_e \sim 10^3$ and $n_e \sim 10^4$ cm^{-3}, giving a flux ratio of Pfα/pfβ$\sim$ 1.81 (D. Hummer & P. Storey 1987).

3.5 VLT/SINFONI data

We supplement our *JWST* observations with archival near-IR VLT/SINFONI (F. Eisenhauer et al. 2003) data of NGC 7582, providing additional constraints on shock modelling through rovibrational H_2 line measurements in SF 1 and SF 2. The SINFONI data cube (PROGRAM ID 093.B-0057, PI: R. Davies) was reduced using the custom SPRED package (R. Abuter et al. 2006), with additional steps to remove the nightsky OH airglow emission (R. I. Davies 2007). These data were originally published and discussed in detail by M.-Y. Lin et al. (2018) (see also references therein). We corrected these data for extinction following D. Calzetti et al. (2000), and comparing the Brγ flux to the Pfβ flux in each aperture under the assumption of case B recombination (D. Hummer & P. Storey 1987).

4 RESULTS AND DISCUSSION

An initial inspection of the combined NIRSpec and MIRI/MRS spectra in the various apertures (Fig. 2) shows that SF 1 and SF 2 are remarkably similar, both exhibiting relatively high continuum flux compared to the other non-nuclear apertures. The main difference between them is that SF 2 displays a more steeply rising MIR continuum beyond $\lambda > 18$ μm. This is consistent with our extinction analysis (Table A1), which indicates a slightly higher dust column towards SF 2. This excess mid-IR emission may also be related to the position of SF 2 along the edge of the ionization cone (Fig. 1), where enhanced dust heating could further boost its long wavelength continuum. In contrast, SF 3 exhibits a distinctly different spectrum: its continuum flux is much lower, and the shapes of its spectral features differ from those of SF 1 and SF 2. This divergence is notable because SF 3 also lies within the circumnuclear star-forming ring, showing that star-forming regions within the same ring (i.e. likely forming from the same gas) can display markedly different physical conditions.

All H_2 $\nu = 0$–0 rotational lines from S(1) to S(7) were detected in each aperture with a signal-to-noise ratio (S/N) greater than 5, except in the nucleus where the S(7) 5.511 μm line is significantly blended with the [Mg VII] 5.503 μm emission line. This metal line is detected only in the nuclear aperture due to having a high ionization potential (IP) of 187 eV. The measured fluxes (extinction-corrected) and associated uncertainties for all H_2 $\nu = 0$–0 lines from S(1) to S(7) in each aperture are presented in Table 1. Some higher J rotational lines, such as the H_2 $\nu = 0$–0 S(8) 5.053 μm, S(9) 4.695 μm and S(10) 4.410 μm lines lie within the NIRSpec range, but are not detected with adequate S/N in the majority of apertures and so were excluded from our analysis.

We also calculate different mid-IR flux ratios from various other emission lines, these are given for every aperture in Table. 2 and are discussed in context with their utility in Section 4.5.

4.1 H_2 rotational line emission and kinematics maps

Fig. 3 presents the line emission and kinematic maps for the rotational S(1), S(3), and S(5) transitions. These lines trace molecular gas at progressively higher kinetic temperatures as J increases, making their comparison particularly useful for identifying regions of elevated gas temperatures. The overall spatial extent of the emission decreases with increasing J, indicating that the cooler phase molecular gas has a more extended distribution. Notably, only the nucleus, SF 1, and SF 2 exhibit substantial emission in the higher excitation S(5) line, strongly indicating that these regions contain a significant fraction of the warmer molecular gas. The S(5) map also reveals quite striking extended emission both north and south of the nucleus, but notably not aligning with the ionization cone as shown in Fig. 1. However, the S(5) emission almost forms a reverse 'S'-shape that encompasses SF 1 and SF 2 in the south and SF 3 in the north, with the inner part of the 'S' loosely following the direction of the proposed jet (Fig. 1).

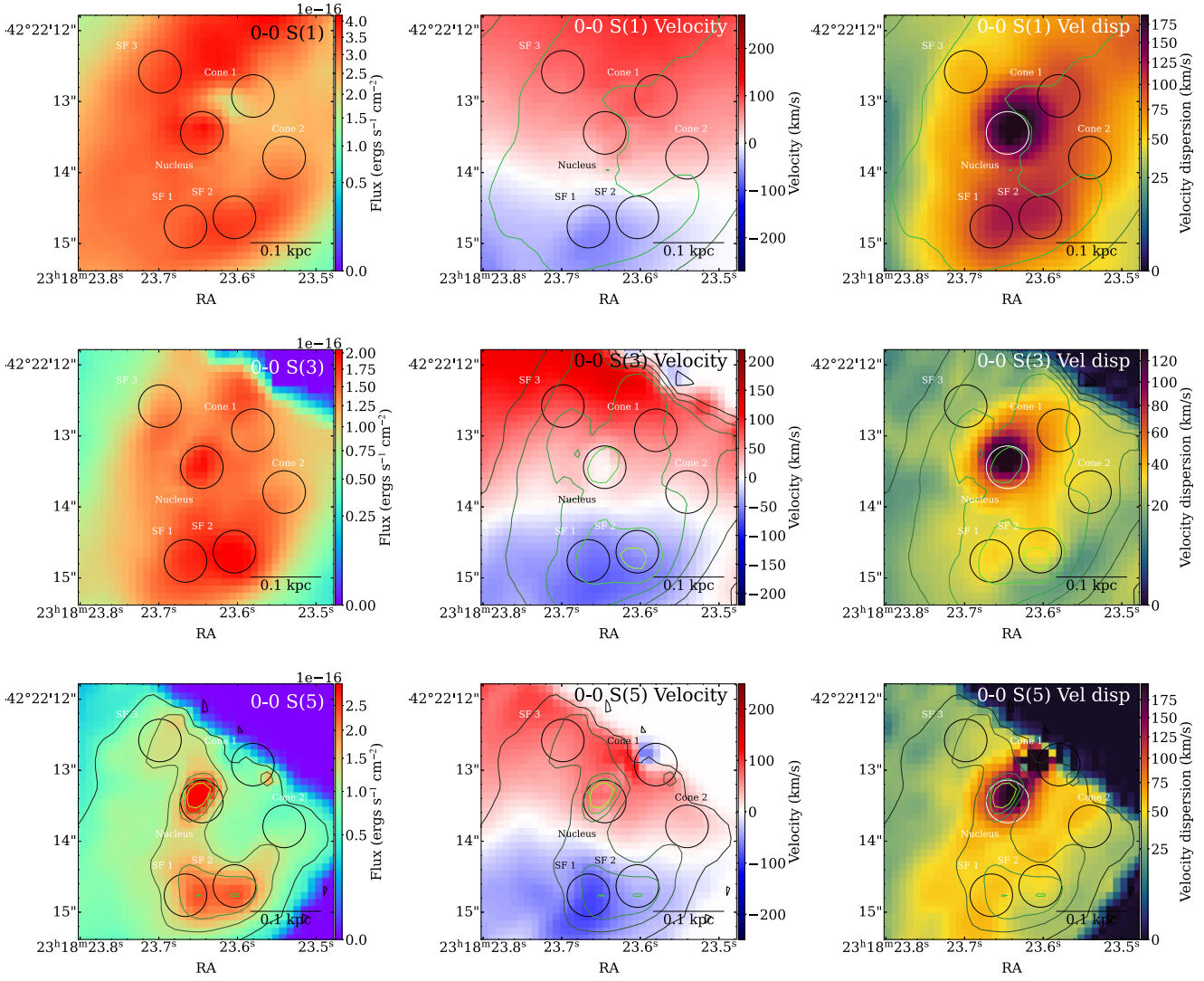

Figure 3. Flux emission, velocity and velocity dispersion maps for H_2 0–0 S(1), S(3) and S(5). Contours show the respective flux line emission. As J increases, the emission lines are tracing warmer molecular gas. This shows that the nucleus, SF 1, and SF 2 contain more warmer molecular gas than any other region.

The kinematic maps for the rotational lines presented in Fig. 3 also reveal several intriguing features. The velocity and dispersion maps for the S(1) and S(3) lines display a notably similar morphology, with SF 1 and SF 2 exhibiting significantly larger velocity dispersions compared to most other circumnuclear spaxels. Additionally, SF 1 and SF 2 (particularly SF 1) appear slightly more blueshifted in the S(1), S(3), and S(5) lines relative to their surrounding spaxels on the approaching side of the galaxy. This additional blueshifting around SF 1 and SF 2 was also detected by S. García-Burillo et al. (2021) in the CO kinematics with ALMA, who linked it to density-wave driven non-circular outflows from the AGN intermediate line region. This combination of enhanced dispersion and blueshifting suggests that SF 1 and SF 2 are considerably more kinematically disturbed in molecular H_2 than other regions. An additional feature is seen uniquely in the S(3) velocity map, where the nucleus shows enhanced blueshifting relative to its immediate surroundings. This blueshift extends southwards toward SF 1 and SF 2, potentially tracing an outflow, although it is interesting we do not see such a strong feature in the S(1) or S(5) kinematics.

The S(5) velocity dispersion map shows significantly elevated dispersion across the nuclear region, with a clear asymmetry between the northern and southern sides. Notably, the dispersion is enhanced around the nucleus compared to throughout the ring, suggesting additional turbulent contributions from shocks or outflows acting in this region.

Collectively, the S(5) kinematics follows a similar pattern to those of the cooler S(1) and S(3) lines, albeit with extended enhanced velocity dispersion south of the nucleus. These results reinforce the conclusions drawn from the emission maps: the warmer molecular gas exhibits a more complex and disturbed morphology, particularly around and south of the AGN, as evidenced by distinct kinematic signatures, which could suggest the presence of shocks.

We also present the velocity profiles of the S(1), S(3), and S(5) lines along PA $= 0°$ (approximately aligned with the major velocity axis) in Fig. 4. We see the clear redshifted offset, particularly in S(1) and S(5) around the nucleus. In contrast, S(3) displays increased scatter near the nucleus and a velocity trend closer to the systemic velocity, consistent with the additional nuclear blueshifting seen in

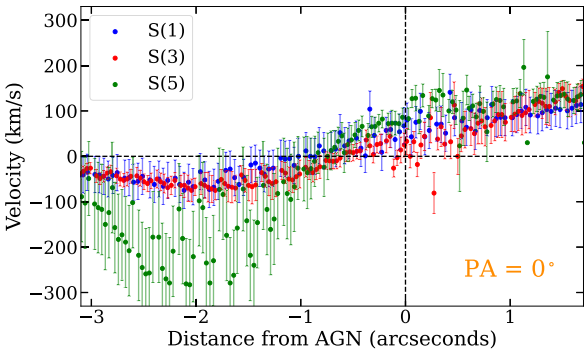

Figure 4. Velocity fit for each spaxel along a pseudoslit of width 3 pixels along PA $= 0°$ for the rotational lines S(1), S(3), S(5).

Fig. 3. Between approximately −3 and −1 arcsec, S(5) also shows enhanced blueshifting that aligns with the blueshifted structure over SF 1 observed in Fig. 3.

4.2 H_2 excitation modelling

A possible H_2 excitation mechanism is shocks as outlined by M. G. Burton, D. Hollenbach & A. Tielens (1992), who demonstrated that H_2 rotational transitions can be efficiently excited by slower shocks compared to those responsible for the near-IR vibrational H_2 emissions. Their work also highlights the dependence of the S(1) line intensity on the temperature of the photodissociation region (PDR), with significant excitation occurring only when $T \gtrsim 100$ K, assuming a fixed ortho-to-para H_2 ratio (OPR) of 3:1 and local thermal equilibrium (LTE).

Since the higher-order S(J) transitions require greater energy, and hence hotter PDRs, to be appreciably excited compared to S(1), we adopt this lower cutoff of $T \gtrsim 100$ K as the baseline for the temperature range probed in our analysis. The wavelength coverage of our NIRSpec G395H/F290LP observations precludes the observation of vibrational H_2 lines, which are better tracers of hotter gas ($T \gtrsim 1000$ K) due to their higher excitation temperatures. Consequently, the kinetic temperature range of the molecular gas that we can reliably constrain using the mid-IR S(1) to S(7) lines is approximately $100 \lesssim T \lesssim 1000$ K, with only a small fraction at hotter temperatures probed only by vibrational lines (A. Togi & J. D. T. Smith 2016).

To model the fluxes of the rotational H_2 lines, we adopt the formalism outlined in M. G. Burton et al. (1992), M. Pereira-Santaella et al. (2014), L. H. Jones et al. (2024), and A. Togi & J. D. T. Smith (2016) (hereafter TS16). We refer the reader to these works for a comprehensive discussion of the theoretical framework. In essence, we assume that the populations of the different rotational energy levels – characterized by their column densities, N, follow a continuous power-law distribution determined by the molecular gas temperature, under the assumption of local thermal equilibrium (LTE). This distribution is given by:

$$\mathrm{d}N = mT^{-n}\mathrm{d}T. \quad (1)$$

Here, m is a scaling coefficient which can be easily found by integrating equation (1) over the total H_2 column density, $N_{\rm tot}$, between upper and lower bounds of the temperature distribution. Importantly, n represents the power-law index. Physically, a larger n (so a more negative exponent overall) results in a steeper decline in the population of higher energy rotational levels, indicating that a greater fraction of the molecular H_2 resides in the lower energy states. This manifests as relatively higher observed fluxes in the lower rotational transitions, such as S(1) and S(2). Conversely, a smaller n (less negative exponent) leads to enhanced fluxes in the higher transitions, such as S(6) and S(7). The power-law distribution is constrained by the lower and upper temperature limits, T_l and T_u, respectively. These do not correspond to physical kinetic temperatures of the molecular gas, rather the integration limits that make the power-law distribution finite and physically interpretable. For rotational line analyses, it is standard practice to adopt a fixed upper limit of $T_u = 2000$ K, as populations at higher temperatures contribute negligibly to the observed flux distribution. This assumption is well-supported in the literature (TS16) and is confirmed by our own calculations of the total H_2 column density. We find that varying T_u beyond 2000 K has an insignificant impact on the derived level populations and the resulting flux.

The lower temperature cutoff parameter, T_l, has a more significant influence on the derived results, as the bulk of the H_2 mass occupies lower energy states associated with these rotational transitions, thus are predominantly excited at relatively low temperatures. An important question, however, becomes: just how low can the lower temperature cutoff be before the S(1) emission becomes undetectable? Consequently, the choice of T_l significantly affects the inferred H_2 column density and must be handled with care. M. G. Burton et al. (1992) demonstrated that assuming a fixed ortho-to-para ratio of 3:1 is reasonable for temperatures $\gtrsim 300$ K. Additionally, since the lowest detectable line in our MIRI/MRS observations is the S(1) transition – which itself is poorly excited at temperatures $\lesssim 150$ K – we feel that adopting a fixed T_l within this range is reasonable. Therefore, we also investigate applying a fixed $T_l = 300$ K when fitting the power-law model, which would be close to the expected T_l for an ortho-to-para ratio of 3:1 for these lines. To assess the robustness of this assumption, we also perform fits without fixing the ortho-to-para ratio, allowing T_l to vary freely. As we demonstrate later, most regions naturally converge toward a best-fit T_l close to 300 K, supporting the validity of our assumption. A detailed theoretical analysis of potential deviations from this ratio, while potentially insightful, lies beyond the scope of this study.

Unfortunately, the lowest-energy rotational H_2 line, S(0) at 28.221 μm, lies beyond the wavelength coverage of MIRI/MRS (28.1 μm) and therefore cannot be included in our analysis.

4.3 Excitation diagrams

All of our TS16 power-law models are generated using the `H2Powerlaw` PYTHON implementation[1]. We construct excitation diagrams, whereby measured fluxes of H_2 rotational lines are converted into column densities and are plotted against the energy of the upper state of the line transition, allowing us to analyse the temperature distribution of the molecular gas in each aperture region. The theory behind modelling excitation diagrams from H_2 rotational line flux observations is discussed for completeness in the Appendix A1.

We fit the excitation diagrams for every aperture region using both the power-law distribution model and an alternative fit that assumes the molecular H_2 resides at a single, fixed temperature. The latter, provides a convenient linear fit on the excitation diagram and allows the column density to be directly inferred from the intercept with the normalized column density axis. These fixed-temperature models have also been employed in previous studies (D. Rigopoulou et al.

[1] https://github.com/astrolojo/H2Powerlaw

Table 3. Best fit n and T_l from our TS16 modelling, as well as the derived H_2 column density and mass for $T > 300$ K for each region. Hotter regions exhibit overall lower n combined with higher T_l.

Region	n	T_l (K)	log N_{H_2} (cm^{-2})	log M_{H_2} ($M_\odot$)
Nucleus	5.6 ± 0.9	330 ± 50	21.45 ± 0.17	5.18 ± 0.17
SF 1	6.5 ± 0.4	310 ± 20	21.14 ± 0.07	4.87 ± 0.07
SF 2	5.9 ± 0.2	280 ± 20	21.32 ± 0.06	5.01 ± 0.06
SF 3	7 ± 2	220 ± 30	21.09 ± 0.33	4.82 ± 0.33
Cone 1	4.8 ± 0.2	140 ± 40	21.34 ± 0.34	5.07 ± 0.34
Cone 2	8 ± 1	270 ± 40	20.64 ± 0.17	4.37 ± 0.17

2002; H. Roussel et al. 2007; M. Rosenberg, P. Werf & F. Israel 2013; R. Davies et al. 2024; D. Esparza-Arredondo et al. 2025; C. Ramos Almeida et al. 2025). The excitation diagrams, constructed from the measured fluxes listed in Table 1 and normalized by the S(1) flux for each aperture, along with the corresponding fits for the three different models, are presented in Fig. 5. The individual rotational diagrams for each aperture with every model plotted separately are shown in the appendix Fig. A1. Finally, the best-fitting T_l and n, along with the inferred H_2 column densities and H_2 mass of each region are given in Table 3.

The TS16 power-law model with a varying ortho-to-para ratio, shown in the top panel of Fig. 5, provides the best fit among all tested models. However, the physical implications of such fits are complicated as variable ortho-to-para ratios remain poorly understood theoretically (M. G. Burton et al. 1992; A. Sternberg & D. A. Neufeld 1999; J. Takahashi 2001). For every model, the best fits are those for the nuclear, SF 1, and SF 2 regions, which is expected given that these exhibit the strongest line fluxes and the highest S/N. As shown in the middle panel of Fig. 5, models with a fixed lower temperature limit of $T_l = 300$ K provide a good fit within one standard deviation for all three of these regions, suggesting that an ortho-to-para ratio of 3:1 is a reasonable assumption. This allows us to confidently fix T_l and focus on comparing the resulting power-law indices, n, instead.

Overall, when keeping T_l fixed, the nucleus has the lowest n, (middle panel of Fig. 5), corresponding to a larger proportion of hot molecular H_2 gas, which is perhaps not unexpected. More intriguing is the fact that SF 1 and SF 2 have very similar n values, which are only slightly higher than that of the nucleus but significantly smaller than those of Cone 1, Cone 2, and SF 3. This suggests that SF 1 and SF 2 have a similar proportion of hot molecular gas as the nucleus which is somewhat puzzling. This observation is further supported by the results in the top panel of Fig. 5, where the best-fitting T_l values for the nucleus, SF 1, and SF 2 are virtually identical within the error bars, as are the corresponding n values. When allowing the ortho-to-para ratio to vary within the power-law distribution, the inferred temperature distributions for these three regions are also indistinguishable within the error margin. This is particularly remarkable given that the star-forming regions are clearly spatially resolved and located about 100 pc away from the nucleus (i.e. not strongly within the PSF even if our corrections were not applied), making it unlikely that nuclear contamination is responsible for their heating.

Furthermore, the bottom panel of Fig. 5 presents the best-fitting discrete temperature model for each aperture, showing the same trend where the nucleus, SF 1, and SF 2 are much hotter than the other regions, as shown by having the least steep gradients. Once again, the results from fitting the discrete temperature model suggest that

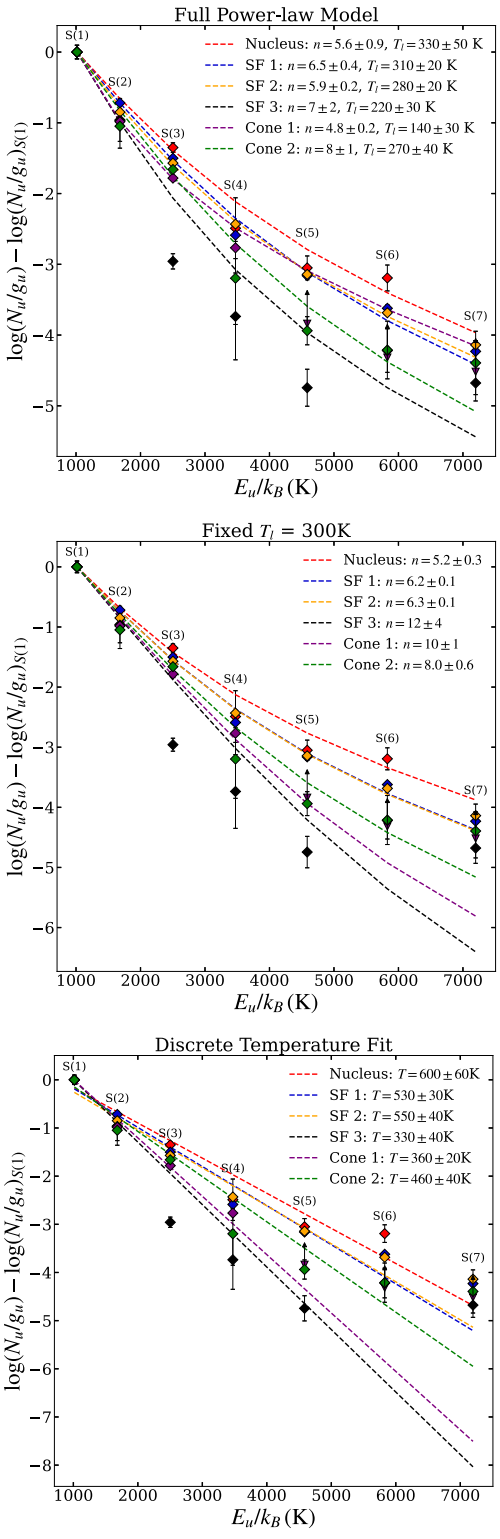

Figure 5. H_2 excitation diagrams for each aperture with three model fits. Top: Power-law temperature distribution with a free OPR. When including rotational lines down to S(1), a best-fitting $T_l \sim 300$ K approximately corresponds to an OPR of 3:1. Middle: Power-law temperature distribution with the OPR fixed to 3:1, leaving n as the sole free parameter. Bottom: Single-temperature model, where the only free parameters are the excitation temperature, T, and the total H_2 column density. A small portion of the Cone 1 aperture extends beyond the MIRI/MRS FOV for S(5), S(6), and S(7), hence these line fluxes are lower limits which we show as triangular markers.

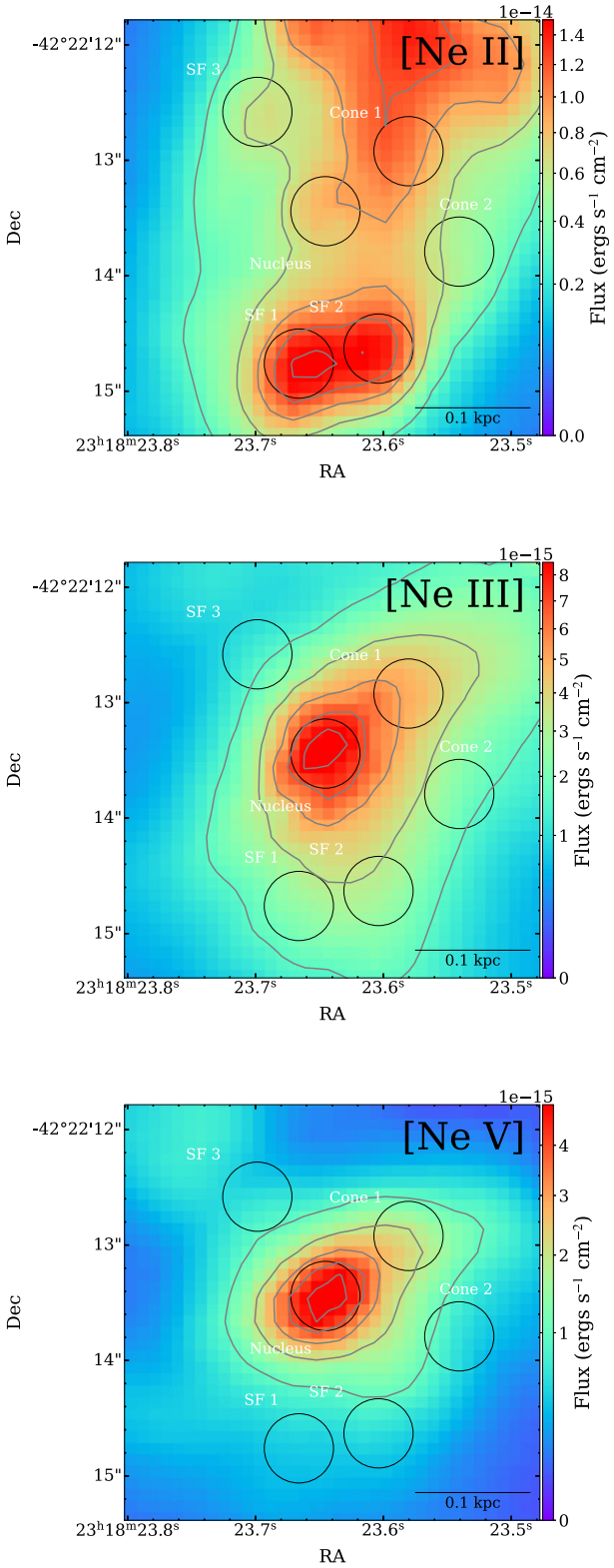

Figure 6. Top to bottom: [Ne II] 12.8 μm, [Ne III] 15.8 μm, [Ne V] 14.3 μm flux maps. [Ne V] is a high ionization line, IP = 97 eV map: there is no increase in its emission in SF 1 or SF 2, supporting the notion that they are not photoionized by the AGN.

SF 1 and SF 2 are at nearly the same temperature as the nucleus, further supporting the conclusions drawn from the power-law fits.

Cone 1, Cone 2, and SF 3 exhibit lower S/N in the higher J lines, resulting in larger scatter of the S(3)–S(7), data points that deviate from the line fit trends of the lower-J transitions. The excitation diagram for SF 3, in particular, is not well fit by any of the models considered here. This is because SF 3 is fainter and has comparatively poor S/N in rotational line fluxes. SF 3 was included as an additional star-forming region for comparison with the more pronounced and intriguing SF 1 and SF 2. Although a comparison of the excitation diagrams of the northern star forming clumps M3, M4, or M5 would have been informative, we note that these regions are only partially covered by the MIRI FOV, hence the study of their H_2 properties is not possible. None the less, the H_2 column density derived for SF 3 reveals a significantly cooler temperature distribution, despite its close proximity to the AGN, supporting our conclusion that the temperature of the molecular gas in SF 1 and SF 2 is unexpectedly elevated. Such H_2 excitation temperatures are not just higher compared to other regions in this galaxy, but also compared to studies of other nearby galaxies (e.g. A. Togi & J. D. T. Smith 2016; S. Hernandez et al. 2023; R. A. Riffel et al. 2025). In the following subsection, we delve deeper into these two regions to further investigate their properties and explore the mechanisms that might be responsible for the gas heating.

4.4 Analysis of the properties of the circumnuclear ISM through mid-IR lines

To investigate the origin of the heating mechanism, we extend our analysis beyond just the H_2 lines, considering additional mid-IR lines and line ratios as diagnostic tracers.

It is well established that [Ne II] line emission traces star formation, [Ne III] can arise from both stellar photoionization and AGN photoionization, whereas [Ne V] requires highly energetic ionising photons, and is only excited by AGN. Fig. 6 shows maps of the [Ne II], [Ne III], and [Ne V] lines for NGC 7582. It is evident that strong [Ne V] emission is entirely confined to the nucleus, with much weaker, morphologically distinct detections in the western side of the ionization cone, clearly visible in the contours shown in the same figure as an extension westward from the nucleus. In SF 1, the [Ne V] line appears as a weak, single-Gaussian component with a flux of order ∼1 per cent that of the nucleus and, critically, with an identical central wavelength to the nucleus. Given that SF 1 is kinematically offset from the nucleus (typically blueshifted), any intrinsic [Ne V] emission would be expected to appear at a different wavelength. The identical line centres therefore indicate this signal is due entirely to PSF contamination from the nucleus. SF 2 shows a similar nuclear PSF feature, but with an additional, weaker blueshifted [Ne V] component. This results in a subtle double-Gaussian line shape and suggests a small amount of genuine [Ne V] emission, possibly originating from SF 2 itself. This is consistent with its location on the southern edge of the western ionization cone (Fig. 1). However, this component is minor and overall the [Ne V] flux is greatly outshone by the nearby [Cl II] 14.36 μm line, a reliable tracer of star formation, which is much stronger in both SF 1 and SF 2, and almost absent in the nucleus. These findings are consistent with the [Ne V] emission being powered by the AGN. The analysis of these lines suggests that the molecular gas in SF 1 and SF 2 is not being heated through direct AGN photoionization.

[Mg IV] 4.487 μm is also a tracer of high ionization (IP = 80 eV). We present the [Mg IV] emission map in Fig. 7, with unsurprisingly the absence of strong [Mg IV] emission in SF 1 and SF 2 or

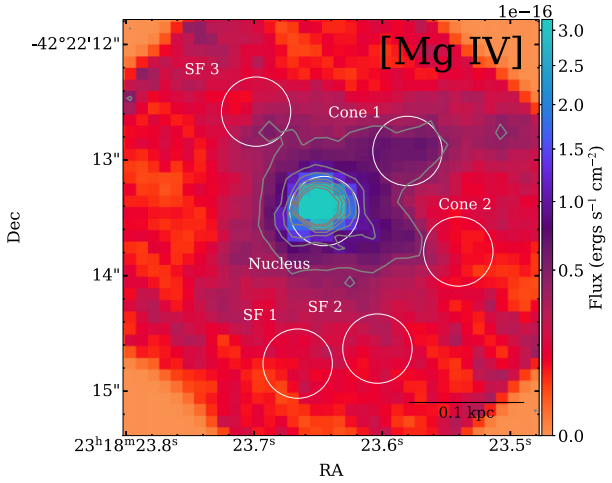

Figure 7. [Mg IV] 4.487 μm flux map tracing gas that is highly ionized. IP = 80 eV. The emission is concentrated in the nucleus and around the edges of the ionization cone.

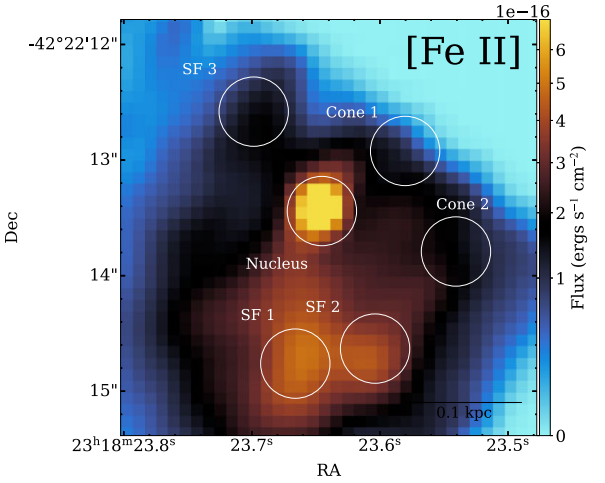

Figure 9. [Fe II] 5.34 μm flux map tracing low-IP shocked gas (IP = 7.9 eV). We see clear extended emission around SF 1 and SF 2, suggesting then that shocks could be heating them.

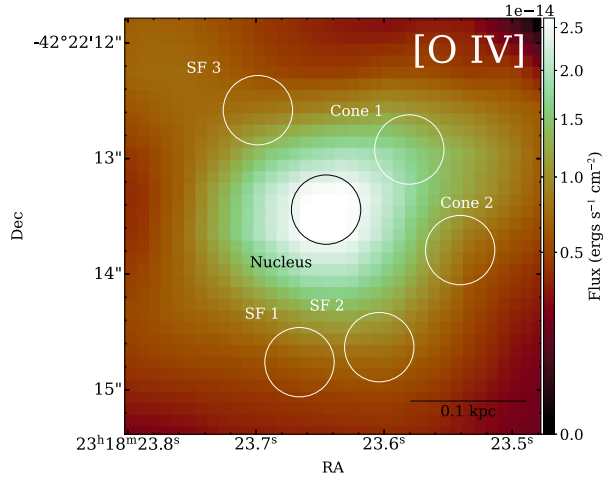

Figure 8. [O IV] 25.89 μm flux map tracing the AGN region and potentially O-type star clusters, showing little evidence that SF 1 and 2 could be being heated by either of these scenarios. We note that the nucleus produces a large PSF, as this line falls within the longest MIRI/MRS wavelength channel.

anywhere south of the nucleus providing further evidence against direct ionization by the AGN, Notably, [Mg IV] emission does appear to trace the edges of the ionization cone, as indicated by the contours in Fig. 7, aligning well with previous literature on the western-facing cone, confirming that it contains strongly ionized gas as expected. Moreover, the [Mg IV] distribution closely resembles that of [Ne V], being confined to the AGN and the western cone edges. The lack of any additional [Mg IV] extension beyond [Ne V] suggests that both lines trace the same ionized gas and are excited by the same mechanism–photoionization by the AGN, as is well established for [Ne V].

The [O IV] 25.89 μm line (IP = 54.9 eV) is a well established tracer of AGN activity as well as the presence of young, hot, massive O-type stars (M. D. Thornley et al. 2000; M. Pereira-Santaella et al. 2010; A. Alonso-Herrero et al. 2011). In NGC 7582, this line is detected by MIRI/MRS with a high S/N ratio. We present its spatial distribution in Fig. 8. We see no morphologically pertinent [O IV] emission beyond the nucleus, suggesting that SF 1 and SF 2 are not influenced by the AGN. The spatial extent of [O IV] flux around the nucleus appears large due to the broad PSF of MIRI/MRS channel 4, where this line is detected. While SF 3, Cone 1, and Cone 2 appear contaminated by nuclear [O IV] flux, SF 1 and SF 2 are much less affected, reinforcing the conclusion that their elevated temperatures are not due to AGN photoionization or a result of PSF contamination from the nucleus.

The [Fe II] 5.34 μm line, which has a low ionization potential of only 7.9 eV, is useful as a well-established diagnostic for low-ionization shocked gas (K. Kawara, M. Nishida & Y. Taniguchi 1988; D. A. Forbes & M. J. Ward 1993). The corresponding map, along with the aperture locations, is presented in Fig. 9. The nucleus exhibits significant [Fe II] emission, indicative of strong AGN activity (J. A. Baldwin et al. 2004). More notably, there is a strikingly clear extension of [Fe II] flux south by south–east of the nucleus, encompassing both SF 1 and SF 2, while no similar directional increase is observed elsewhere; however, the MIRI/MRS FOV for this line does not extend to the northern regions of the star-forming ring, preventing us from determining whether the northern star-forming clumps, M3, M4, M5, also show enhanced [Fe II] 5.34 μm emission. None the less, this provides evidence that SF 1 and SF 2 may contain substantial shocked gas, which could be the cause of their observed higher than expected H_2 temperatures.

T. Ricci et al. (2018) reported strong near-IR [Fe II] 1.64 μm emission in the nucleus, also extending along a position angle of $\sim 20°$, aligning with Fig. 9. The southern [Fe II] extension across SF 1 and SF 2 may arise from an AGN jet interacting with the surrounding ISM. As the jet disrupts, it could lose collimation and disperse into a broader outflow, driving shocks that compress, fragment, and entrain ambient gas, thereby enhancing [Fe II] emission. T. Ricci et al. (2018) further showed that any such jet would be nearly orthogonal to the ionization cone, traced by the Brγ hydrogen recombination line in the near-IR. However, we find no clear evidence of this jet in our Pfβ recombination map (Fig. 1), nor in other lines such as Pfα or Brα.

Furthermore, T. Ricci et al. (2018) proposed that SF 2 may be photoionized by the ionization cone, given its position along the southern edge of the western-facing cone. We conclude that although SF 2 likely experiences some small additional photoionization from the cone, the molecular gas in both regions is primarily shock heated. [SF 2 shows weak high-ionization features (e.g. [Ne V]), weak Brα

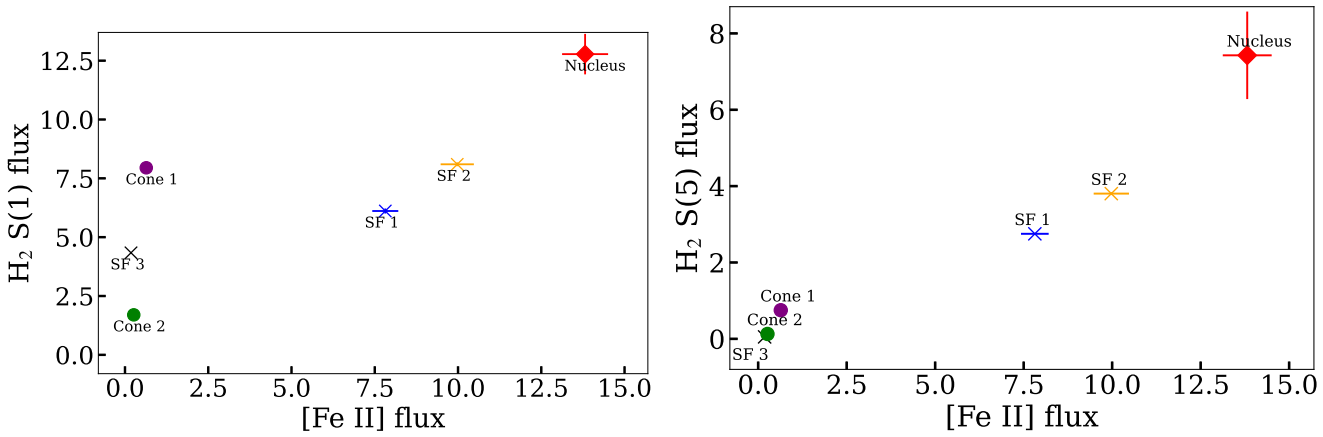

Figure 10. H_2 rotational line vs [Fe II] 5.34 μm flux (in units of 10^{-15} erg s^{-1} cm^{-2}). Left: S(1) transition, right: S(5) transition.

emission, and identical molecular gas temperature and excitation to SF 1.]

We also compare the amount of [Fe II] to H_2 flux in Fig. 10. Both [Fe II] versus S(1) (left) and [Fe II] versus S(5) (right) display linear correlations across the selected aperture regions (but we note that in the left panel the correlation appears to be driven in part by the nucleus, and without this point the trend is less pronounced). This indicates a physical connection between shocked gas traced by [Fe II] and the warm molecular gas. The correlation is strongest for the S(5) line, which probes higher excitation temperatures, suggesting that the warmest H_2 is most closely linked to [Fe II] emission, thus further supporting shock excitation as the dominant heating mechanism in these regions.

Significant [Fe II] emission can also arise from photoionization by star formation and AGN activity. For example, NGC 4303 exhibits a star-forming ring bright in [Fe II] emission (R. A. Riffel et al. 2016), as does NGC 7469 (M. Bianchin et al. 2024), and numerous other galaxies with circumnuclear star formation. Photoionization models are capable of reproducing [Fe II] emission even in the absence of coronal line emission (O. L. Dors et al. 2012), as the ionization potential of [Fe II] is relatively low, allowing diffuse AGN photons to contribute significantly. A common method to distinguish [Fe II] emission caused by shocks from that due to photoionization is through diagnostic line ratios, particularly comparing [Fe II] to hydrogen recombination lines in near-IR diagrams (L. Colina et al. 2015). For this purpose, we consider the [Fe II] 5.34 μm/Pfα ratio as it serves as an established shock sensitive tracer in the mid-IR (D. Hollenbach & C. F. McKee 1989; U. Vivian et al. 2022). We provide this ratio in Table 2. A. Alonso Herrero et al. (2025) compared this ratio in many different regions of Seyfert nuclei and low luminosity AGNs and demonstrated that shocked regions typically exhibit $\log_{10}$[Fe II]/Pf$\alpha \gtrsim 0.7$. While all regions show ratios consistent with potential shocks, we caution that the large uncertainties, due to the low S/N of Pfα, limit the robustness of this diagnostic outside SF 1 and SF 2. However, for SF 1 and SF 2, where Pfα is measured with high S/N, this ratio is consistent with the presence of shocks in these regions.

[Mg IV] has also been shown to be a tracer of shocked gas in highly ionized regions (M. Pereira-Santaella et al. 2024), and as we see no clear extension south of the nucleus compared to [Fe II], this suggests that these shocks would likely be low ioni,zation and low velocity.

4.5 Shock models

In this subsection, we employ the well-established Paris-Durham models (D. R. Flower, G. Forêts & T. W. Hartquist 1985; D. R. Flower & G. Forêts 2003) to investigate a shock origin for the observed H_2 emission. The input energy flux, both radiative and kinetic, from a potential shock can be reprocessed and emitted as H_2 rovibrational and/or rotational line emission. Different types of shocks produce distinct ratios and fluxes of rotational and vibrational H_2 lines (L. Kristensen et al. 2023). Shocks with velocities exceeding 30 km s^{-1} significantly dissociate H_2, causing its abundance to decrease sharply. This does not by itself rule out the shock origin; for instance, a lower velocity shock could still arise from an AGN jet propagating through a clumpy medium, where interactions cause the jet to split and redirect across a range of velocities (D. Mukherjee et al. 2016, 2018).

L. Kristensen et al. (2023) discuss the application of shock models using *JWST* data and highlight various diagnostics for Paris–Durham models, as outlined by B. Godard et al. (2019), including the use of H_2 lines. They suggest that the primary parameters influencing the type of shock present and the resulting distribution of H_2 line fluxes are the proton number density, n_H, the hardness of the radiation field, characterized by the UV field strength G_0, the shock velocity, v_s, and the strength of any potential magnetic field, quantified by the scaling factor b, where $B = b \times \sqrt{n_H(\mathrm{cm}^{-3})}$ μG. Additionally, the models have minor dependencies on the cosmic H_2 ionization rate, ξ_{H_2}, and the fractional abundance of PAHs relative to hydrogen, X(PAH).

The models predict that higher velocity shocks, or shocks in stronger magnetic fields, typically correspond to C-type (continuous) shocks, whereas lower velocity shocks, or shocks in weaker magnetic fields, are more likely to be J-type (jump) shocks. This distinction between shocks leads to a larger proportion of the shock energy being dissipated via pure rotational transitions of excited H_2 in C-type shocks. They suggest that in a C-type shock, with the same input energy as a J-type shock, a stronger magnetic field causes the neutral and ionized fluids to decouple. This results in the sound speed in the medium being lower than the ion-magnetosonic speed, thus creating a magnetic precursor ahead of the shock front. Overall, C-type shocks excite H_2 to kinetic temperatures of $\sim 10^3$ K, whereas J-type shocks excite it to $\sim 10^4$ K, hence leading to larger vibrational line fluxes in J-type shocks compared to rotational.

L. Kristensen et al. (2023) emphasize that analysing rotational lines alone often leave shock models degenerate. To address this,

several studies (e.g. R. Davies et al. 2024; Delaney et al., submitted) combine *JWST* data with ground based near-IR observations of higher energy H_2 vibrational lines (e.g. 1–0 S(1), S(2), S(3)) to constrain plausible shock models. We adopt a similar approach, incorporating archival VLT/SINFONI rovibrational line fluxes together with additional ISM parameter modelling of the PDR, enabling us to select a non-degenerate and more robust shock model.

To better constrain the properties of the ISM we use the PhotoDissociation Region Toolbox, `pdrtpy`[2] (M. W. Pound & M. G. Wolfire 2022), which constrains physical conditions in PDRs. The PDR models span a range of $n_{\rm H}$, and G_0, assuming no magnetic fields. By inputting at least three line ratios, the intersection of model contours provides the best-fitting values of $n_{\rm H}$ and G_0. This is shown graphically in Fig. 11 using line fluxes for 0–0 S(1), S(2), and S(3) in the nuclear, SF 1, and SF 2 apertures. This analysis yields the same two distinct solutions of $n_{\rm H} \sim 10^4$ or $\sim 10^{5-5.5}$ cm^{-3} and $G_0 \sim 10^2$ or $\sim 10^3$ Habing for both SF 1 and SF 2.

Our aim here is not to constrain ISM parameters with high precision, but rather with sufficient accuracy to resolve otherwise degenerate shock models. Although uncertainties of up to an order of magnitude remain, this precision is adequate since different shock models that reproduce similar H_2 excitation diagrams can typically predict ISM parameters differing by more than an order of magnitude. By incorporating independent constraints from PDRToolbox, we can exclude physically unrealistic scenarios and isolate the most plausible shock solution. This step is crucial, as degeneracies can persist even when both rotational and rovibrational lines are considered (R. Davies et al. 2024). The addition of PDRToolbox analysis therefore provides the necessary constraints to break all remaining degeneracies, yielding the most reliable shock solution and parametrization.

We also limit our shock models to those with stronger magnetic fields, $b \gtrsim 1$. NGC 7582 shows prominent radio emission (M. Ward et al. 1980; M. Orienti & M. Prieto 2010) (with SF 2 being identified as region R3 in the latter, with SF 1 the clear extension eastwards of R3), which may drive AGN outflows. Previous radio studies, such as J. Farnes, D. Green & N. Kantharia (2014), revealed that the central region exhibits a high degree of linear polarization, indicative of a significant Faraday depth. The presence of linear polarization suggests that the synchrotron emitting plasma in the nucleus contains a well-ordered magnetic field component, as an entirely random field would result in depolarization of the emission. This polarization is therefore a direct consequence of a strong magnetic field (P. Frick et al. 2011). Quantitatively, these radio studies suggest that magnetic field strengths in the nuclear regions of NGC 7582 are typically $\gtrsim$1 mG, supporting the assumption that $b \gtrsim 1$ even at the inferred densities of $n_{\rm H} \sim 10^6$ cm^{-3}. Consequently, low magnetic field shock models can be reasonably excluded from our analysis. The combination of these constraints, along with the ISM conditions inferred from the PDRToolbox, and the inclusion of rovibrational line fluxes, provides sufficient information to resolve the degeneracy between shock models.

We apply these constraints on our selection of appropriate shock models. Specifically, we require parameters to be roughly within $n_{\rm H} \sim 10^4$–$10^{5.5}$ cm^{-3}, $G_0 \sim 10^2$–10^4 Habing, and restricted to $b \gtrsim 1$. We examine the model grids from the Paris-Durham Shock Code 1.1.0,[3] and compare the predicted H_2 fluxes with those measured in SF 1 and SF 2 for each shock model. We include all well detected

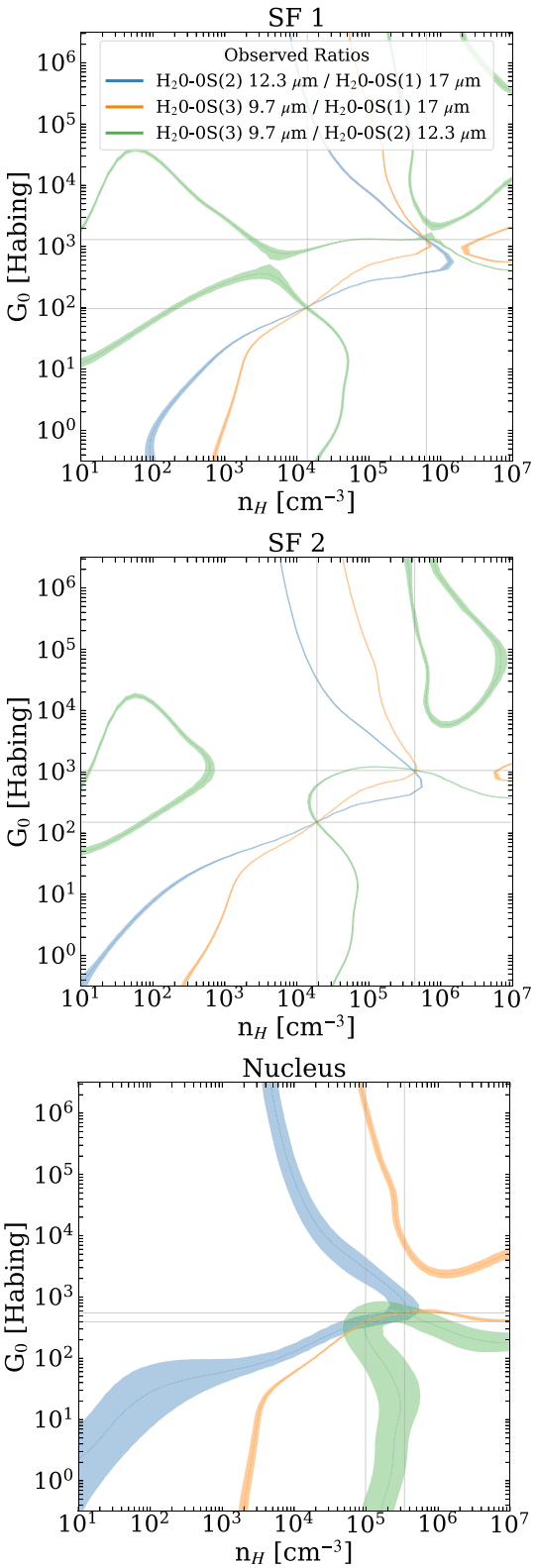

Figure 11. Inferred G_0 and $n_{\rm H}$ for the nucleus, SF 1, and SF 2 from applying The PhotoDissociation Region Toolbox (M. W. Pound & M. G. Wolfire 2022) with the observed three lowest rotational H_2 line ratios (found from inspecting where all three curves intersect). The widths vary due to uncertainties in the measured fluxes for each region. For SF 1 and SF 2, this gives two independent solutions, which only differ by roughly an order of magnitude in their predicted ISM parameters.

[2] https://github.com/mpound/pdrtpy-nb
[3] https://app.ism.obspm.fr/ismdb/

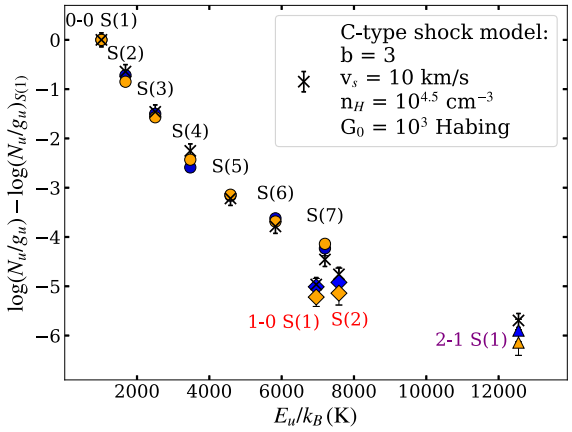

Figure 12. Excitation diagram of SF 1 (blue) and SF 2 (orange) JWST MIRI/MRS H_2 0–0 S(1) to S(7) (circles), and VLT/SINFONI 1–0 S(1), 1–0 S(2) (diamonds), and 2–1 S(1) (triangle) fluxes with the best-fit Paris-Durham Shock Code 1.1.0 model prediction (crosses) with parameter values given in the legend.

rotational lines from *JWST*, 0–0 S(1) to S(7), along with the 1–0 S(1), 1–0 S(2), and 2–1 S(1) rovibrational lines from SINFONI.

We identify only two good fits to all available rotational and rovibrational line fluxes for SF 1 and SF 2, which happen to have nearly identical parameters, differing only in $n_{\rm H}$ by one order of magnitude. These models both correspond to a C-type shock with $b = 3$ and $v_s = 10\,{\rm km\,s^{-1}}$, assuming $G_0 = 10^3$ Habing, $n_{\rm H} = 10^4$ or $10^5\,{\rm cm^{-3}}$, respectively. We acquire our best overall fit model by linearly interpolating between them (as they differ only in $n_{\rm H}$), this is presented in Fig. 12. These results align closely with the ISM conditions inferred from PDRToolbox, showing consistency between all of our analyses, while also predicting a low-velocity shock ($v_s < 30\,{\rm km\,s^{-1}}$), necessary for negligible H_2 dissociation. Furthermore, the presence of a strong magnetic field in this region, as inferred from J. Farnes et al. (2014), supports the plausibility of this shock scenario. The H_2 kinematics in Fig. 3 show elevated velocity dispersions in SF 1 and SF 2, exceeding those in surrounding ISM regions by approximately 10–20 km s^{-1}. This enhancement supports the presence of the best fitting low-velocity shock model, which is responsible for the increased H_2 rotational temperatures observed in these regions.

The shock is of relatively low velocity and does not possess sufficient energy to dissociate H_2 or disrupt the star forming disc. Instead, it primarily acts to elevate the gas temperature, resulting in significantly enhanced H_2 rotational line fluxes. Moreover, the strong nuclear magnetic field plays a crucial role in shaping the shock structure. The presence of a magnetic precursor extends the shock front upstream, distributing kinetic energy over a larger physical scale. This process reduces the energy imparted to individual H_2 molecules, thereby suppressing dissociation while still maintaining sufficient excitation to produce the observed strong rotational transitions.

These results demonstrate that even low energy shocks could significantly influence the thermal and dynamical properties of the surrounding gas. The source of this shock is the focus of the final subsection.

4.6 Is there a jet-ISM interaction in NGC 7582?

Throughout this paper, we have explored various scenarios to explain the observed properties of SF 1 and SF 2, considering whether the observed shock heating is driven by the AGN; either through direct radiation or feedback mechanisms such as the jet proposed by T. Ricci et al. (2018), or by local starburst activity. In this final subsection, we summarize our findings within the context of the ongoing debate about the presence of a jet in NGC 7582.

We emphasize that confirming or excluding a jet ultimately requires radio observations. IR data only allow us to infer its presence through its impact on the ISM rather than direct detection. Hence, the strongest evidence for the AGN jet comes from radio studies (D. A. Forbes & R. Norris 1998; M. Orienti & M. Prieto 2010), which reveal extended emission south of the nucleus. This feature has been interpreted as a possible jet by T. Ricci et al. (2018), who showed that the extended [Fe II] and Brγ emission in the southern regions cannot be explained by the established ionization cone. They identified similar spectral signatures not only in SF 1, SF 2, but also in the northern star-forming clumps (M3, M4, M5), suggesting that these bright IR clusters trace a Seyfert jet rather than simply being dust-embedded. The extended [Fe II] emission further indicates shocks south of the nucleus, consistent with a jet propagating through the surrounding ISM.

Furthermore, in our kinematic analysis of the warm molecular gas (Figs 3 and 4), we observe slight additional blueshifting over the AGN position, especially in S(3), extending southwards across SF 1, roughly aligned with the jet direction proposed by T. Ricci et al. (2018). This blueshift spans a few spaxels, which could result from the PSF smoothing a more narrow kinematic feature produced by an AGN jet. The blueshift also roughly follows the enhanced southern [Fe II] emission (Fig. 9), tracing the shocked gas. Taken together, these features may indicate an AGN jet propagating through the ISM towards the observer and over SF 1 and SF 2, shock-heating the surrounding gas. We note that in a clumpy medium, such as NGC 7582 with its circumnuclear ring hosting multiple star-forming clumps, the AGN jet need not be collimated. While the radio emission may remain collimated, optical or IR counterparts may be absent, as the jet could fragment and redirect multiple times at varying velocities (D. Mukherjee et al. 2016, 2018).

However, these shocks could instead be triggered by cloud–cloud collisions within the intermediate line region that hosts the starburst ring. Such collisions may also account for the non-circular motions seen in CO (3–2) emission (appendix D.1 of S. García-Burillo et al. 2021). To reconcile our findings with other previous work, we argue that many of the 'jet' signatures identified by T. Ricci et al. (2018) are not unique to AGN jets but could also arise from intense starburst activity. Specifically, the observed asymmetries between the northern and southern emission regions pose a significant challenge to the jet hypothesis. For example, our [Fe II] emission map exhibits strong emission only in the south, a trend also noted by T. Ricci et al. (2018) in their near-IR [N I] 5198 and [O I] 6300 line maps. As they discussed, attributing this asymmetry solely to high dust attenuation in the north due to the obscuring disk is insufficient, as the asymmetry is also evident in radio observations (D. A. Forbes & R. Norris 1998), which we also argue appears more diffuse and knotty and not jet like in morphology. The radio maps presented in M. Orienti & M. Prieto (2010) also show clumps of strong radio emission eastwards and northwestwards of the nucleus, which they also attribute to star formation instead of a jet. Hence, the absence of emission extending northwards in many IR lines and in the radio makes it difficult to justify the presence of an AGN jet. However, some of our *JWST* observations do not fully cover the northern edge of the star forming ring. Consequently, while we do not detect [Fe II] emission north of the nucleus in the coverage we do have, this absence does not imply

that shocks or AGN jet impacts are not present further north in the ring.

Emission line flux maps of high IP lines such as [Mg IV] (Fig. 7) and [Ne V] (Fig. 6) reveal emission tracing the edges of the ionization cone but no indication of interaction with a high ionization jet. Furthermore, our low ionization jet tracers; ([Fe II], H_2 S(5), and Pfβ), show enhanced flux over SF 1 and SF 2, but again, no northern counterpart (even when northern FOV is available). Additionally, our PDR modelling indicate that SF 1 and SF 2 exhibit nearly identical ISM conditions. If a jet with the morphology proposed by T. Ricci et al. (2018) were penetrating SF 1 but not SF 2, it would be impossible for both regions to have strikingly similar ISM conditions across multiple tracers.

We propose that the bright, clumpy emission in the southern circumnuclear regions could arise from intense starburst activity. Such vigorous star formation could naturally produce low velocity shocks, without invoking a specific fragmented or redirected AGN jet to explain the similar flux and velocity signatures in SF 1 and SF 2 seen across many emission lines. As these clumps originate from the same gas which forms the circumnuclear ring, it is plausible that they experience comparable star formation histories, consistent with previous studies (M. Wold & E. Galliano 2006; R. A. Riffel et al. 2009), which reasonably accounts for the similar ISM conditions observed. This scenario could also explain the observed north–south asymmetries in emission line distributions, the absence of a northern jet counterpart (within our coverage), all of which argue against a jet-driven origin.

5 CONCLUSIONS

We have presented combined *JWST* NIRSpec and MIRI/MRS 3.87–28.1 μm spectra of the inner nuclear region of the Seyfert 2 galaxy NGC 7582, focusing on the analysis of pure rotational H_2 $\nu = 0$–0 emission lines across multiple apertures. Our main findings are summarized as follows:

(i) Fitting three different LTE models to H_2 rotational lines S(1) to S(7) across six aperture regions consistently demonstrates that the two southern star-forming regions, SF 1 and SF 2, are significantly hotter than the smaller north-eastern star-forming region, SF 3, as well as the regions within the western-facing ionization cone, Cone 1 and Cone 2. The temperature distribution of the warm molecular gas ($\sim 100 < T < 1000$ K) in SF 1 and SF 2 more closely resembles that of the AGN-powered nucleus. The best-fitting model, a power-law temperature distribution without a fixed ortho-to-para ratio, indicates that SF 1, SF 2, and the nucleus share a common lower cutoff temperature ($T_l \sim 300$ K, consistent with an ortho-to-para ratio of 3) and a similar power-law index within one standard error.

(ii) The ionization state of the ISM in the nuclear regions, traced via comparing the [Ne II] 12.8 μm, [Ne III] 15.6 μm, and [Ne V] 14.3 μm flux emission, indicates that only the nucleus is highly ionized, ruling out direct photoionization as a dominant heating mechanism for SF 1 and SF 2. We also see no intrinsic [O IV] 25.9 μm emission in these regions, suggesting that SF 1 and SF 2 are not photoionized by the AGN or any evidence in favour of them being heated by embedded clusters of hot O-type stars either.

(iii) By analysing mid-IR line ratios and H_2 rotational line fluxes with the PDRToolbox, we loosely constrain the ISM conditions in each aperture. The nucleus exhibits the highest ionization, consistent with direct AGN heating, whereas the surrounding star forming regions have lower ionization as expected for star forming regions.

(iv) We look for evidence of shocked gas through spatial mapping of [Fe II] 5.34 μm and [Mg IV] 4.49 μm. The [Fe II] emission exhibits a substantial spatial extension south of the nucleus, covering SF 1 and SF 2, suggesting that low-ionization shocks may be responsible for their increased molecular temperature. We also see a positive correlation between [Fe II] and rotational H_2 flux in each aperture, supporting the idea the two are associated. In contrast, [Mg IV] emission is concentrated within and slightly west of the nucleus, tracing the position of the AGN ionization cone, further supporting the notion that SF 1 and SF 2 are not highly ionized.

(v) Kinematic evidence for shocked gas south of the nucleus shows increased velocity dispersions in rotational H_2 S(1), S(3), and S(5). The S(5) emission shows distinct spatial extent north and south of the nucleus, revealing a mini-spiral of warm molecular gas out to ~ 200 pc.

(vi) A low velocity ($v_s \sim 10\,\mathrm{km\,s^{-1}}$) C-type shock model from the Paris–Durham Shock Code, assuming ISM conditions with a high magnetic field ($b \sim 3$), proton number density ($n_H \sim 10^{4.5}\,\mathrm{cm^{-3}}$), and UV radiation field strength ($G_0 \sim 10^3$ Habing), provides an excellent fit to the observed H_2 rotational and rovibrational line fluxes in SF 1 and SF 2. These ISM conditions are consistent with our PDRToolbox modelling and previous literature studies.

(vii) We investigated whether the observed shocks originate from the AGN jet proposed by T. Ricci et al. (2018) interacting with the ISM or from intense starburst activity. The additional blueshifting around and south of the AGN, as well as elevated velocity dispersions extending over the southern star forming regions of the warm molecular gas kinematics, are consistent with a jet interacting with a clumpy medium. However, the absence of a clear northern counterpart (possibly due to limited spatial coverage), the knotty, diffuse appearance of the radio emission resembling star-forming clumps, the similar ISM conditions in SF 1 and SF 2, all favour starburst driven shocks from gas in the circumnuclear ring. Nevertheless, we cannot rule out either an AGN jet or starburst scenario.

To conclude, this study finds that the southern circumnuclear star-forming regions in NGC 7582 show unexpectedly high molecular H_2 temperatures. Our analysis favours the presence of low-velocity C-type shocks, although the dominant heating mechanism remains unclear. This sheds light on the complex dynamics of circumnuclear discs and underscores the need for multifaceted approaches to disentangle the roles of shocks, radiation, and outflows in AGN environments. We also show that star formation can significantly impact nearby photodissociation regions, altering H_2 excitation and diagnostic line ratios. These results demonstrate *JWST*'s ability to probe feedback processes in unprecedented detail, opening new avenues for studying AGN-impacted galaxy evolution.

ACKNOWLEDGEMENTS

OV is supported by a Science and Technology Facilities Council (STFC) studentship no. ST/Y509474/1. SGB and FE acknowledge support from the Spanish grant PID2022-138560NB-I00, funded by MCIN/AEI/10.13039/501100011033/FEDER, EU. MPS acknowledges support under grants RYC2021-033094-I, CNS2023-145506, and PID2023-146667NB-I00 funded by MCIN/AEI/10.13039/501100011033 and the European Union NextGenerationEU/PRTR. RAR acknowledges the support from Conselho Nacional de Desenvolvimento Científico e Tecnológico (CNPq; Proj. 303450/2022-3, 403398/2023-1, and 441722/2023-7), Fundação de Amparo à pesquisa do Estado do Rio Grande do Sul (FAPERGS; Proj. 21/2551-0002018-0), and Coordenação

de Aperfeiçoamento de Pessoal de Nível Superior (CAPES; Proj. 88887.894973/2023-00). AJB acknowledges funding from the 'FirstGalaxies' Advanced Grant from the European Research Council (ERC) under the European Union's Horizon 2020 research and innovation program (grant agreement no. 789056). SC and DJR acknowledge the support of the UK's Science and Technology Facilities Council (STFC) through grant ST/X001105/1. EB acknowledges support from the Spanish grants PID2022-138621NB-I00 and PID2021-123417OB-I00, funded by MCIN/AEI/10.13039/501100011033/FEDER, EU. CRA, and AA acknowledge support from Agencia Estatal de InvestigaciÅLon of the Ministerio de Ciencia, Innovaci ÅLon y Universidades (MCIU/AEI) under the grant 'Tracking active galactic nuclei feedback from parsec to kiloparsec scales', with reference PID2022-141105NB-I00 and the European Regional Development Fund (ERDF). AA acknowledges funding from the European Union grant WIDERA ExGal-Twin, GA 101158446. EKSH and DD acknowledge grant support from the Space Telescope Science Institute (ID JWST-GO-03535). SFH acknowledges support through UK Research and Innovation (UKRI) under the UK government's Horizon Europe funding Guarantee (EP/Z533920/1) and an STFC Small Award (ST/Y001656/1). AAH and LHM acknowledge support from grant PID2021-124665NB-I00 funded by the Spanish Ministry of Science and Innovation and the State Agency of Research MCIN/AEI/10.13039/501100011033 and ERDF A way of making Europe.

DATA AVAILABILITY

The data cubes used here are publicly available from the Mikulski Archive for Space Telescopes (MAST),[4] with DOI: 10.17909/9sc5-q436.

REFERENCES

Abuter R., Schreiber J., Eisenhauer F., Ott T., Horrobin M., Gillesen S., 2006, New Astron. Rev., 50, 398
Alonso-Herrero A. et al., 2020, A&A, 639, A43
Alonso-Herrero A., Pereira-Santaella M., Rieke G. H., Rigopoulou D., 2011, ApJ, 744, 2
Alonso-Herrero A. et al., 2021, A&A, 652, A99
Alonso Herrero A. et al., 2025, A&A, 699, A334
Argyriou I. et al., 2023, A&A, 675, A111
Armus L. et al., 2023, ApJ, 942, L37
Baldwin J. A., Ferland G. J., Korista K., Hamann F., LaCluyzé A., 2004, ApJ, 615, 610
Bianchi S., Piconcelli E., Chiaberge M., Bailón E. J., Matt G., Fiore F., 2009, ApJ, 695, 781
Bianchin M. et al., 2024, ApJ, 965, 103
Bohn T. et al., 2024, ApJ, 977, 36
Böker T. et al., 2022, A&A, 661, A82
Böker T. et al., 2023, PASP, 135, 038001
Braito V., Reeves J., Bianchi S., Nardini E., Piconcelli E., 2017, A&A, 600, A135
Burton M. G., Hollenbach D., Tielens A., 1992, ApJ, 399, 563
Calzetti D., 1996, AJ, 113, 162
Calzetti D., Armus L., Bohlin R. C., Kinney A. L., Koornneef J., Storchi-Bergmann T., 2000, ApJ, 533, 682
Cappellari M., 2023, MNRAS, 526, 3273
Colina L. et al., 2015, A&A, 578, A48
Costa-Souza J., Riffel R. A., Souza-Oliveira G. L., Zakamska N. L., Bianchin M., Storchi-Bergmann T., Riffel R., 2024, ApJ, 974, 127
Davies R. et al., 2024, A&A, 689, A263
Davies R. I., 2007, MNRAS, 375, 1099
Davies R. I., Sternberg A., Lehnert M., Tacconi-Garman L., 2003, ApJ, 597, 907
Donnan F. R., García-Bernete I., Rigopoulou D., Pereira-Santaella M., Roche P. F., Alonso-Herrero A., 2024, MNRAS, 529, 1386
Dors O., Storchi-Bergmann T., Riffel R. A., Schimdt A. A., 2008, A&A, 482, 59
Dors O. L., Riffel R. A., Cardaci M. V., Hägele G. F., Krabbe Â. C., Pérez-Montero E., Rodrigues I., 2012, MNRAS, 422, 252
Eisenhauer F. et al., 2003, in SPIE 4841 1548
Esparza-Arredondo D. et al., 2025, A&A, 693, A174
Fabian A. C., 2012, ARA&A, 50, 455
Farnes J., Green D., Kantharia N., 2014, MNRAS, 437, 3236
Fletcher T. J., Saintonge A., Soares P. S., Pontzen A., 2021, MNRAS, 501, 411
Flower D. R., Pineau des Forêts G., 2003, MNRAS, 343, 390
Flower D. R., Pineau des Forêts G., Hartquist T. W., 1985, MNRAS, 216, 775
Forbes D. A., Norris R., 1998, MNRAS, 300, 757
Forbes D. A., Ward M. J., 1993, ApJ, 416, 150
Frick P., Sokoloff D., Stepanov R., Beck R., 2011, MNRAS, 414, 2540
García-Bernete I. et al., 2022, A&A, 666, L5
García-Bernete I. et al., 2024, A&A, 681, L7
García-Burillo S. et al., 2021, A&A, 652, A98
Gardner J. P. et al., 2023, PASP, 135, 068001
Godard B., Des Forêts G. P., Lesaffre P., Lehmann A., Gusdorf A., Falgarone E., 2019, A&A, 622, A100
Harrison C., 2017, Nat. Astron., 1, 0165
Harrison C. M., Ramos Almeida C., 2024, Galaxies, 12, 17
Hernandez S. et al., 2023, ApJ, 948, 124
Hicks E., Davies R., Malkan M., Genzel R., Tacconi L., Sánchez F. M., Sternberg A., 2009, ApJ, 696, 448
Higdon S. J., Armus L., Higdon J., Soifer B., Spoon H., 2006, ApJ, 648, 323
Hollenbach D., McKee C. F., 1989, ApJ, 342, 306
Hollenbach D., Tielens A., 1997, ARA&A, 35, 179
Hummer D., Storey P., 1987, MNRAS, 224, 801
Jakobsen P. et al., 2022, A&A, 661, A80
Jones L. H. et al., 2024, ApJ, 987, 17
Juneau S. et al., 2022, ApJ, 925, 203
Kaplan K. F., Dinerstein H. L., Kim H., Jaffe D. T., 2021, ApJ, 919, 27
Kawara K., Nishida M., Taniguchi Y., 1988, ApJ, 328, L41
Kessler M. et al., 1996, A&A, 315, L27
Kristensen L., Godard B., Guillard P., Gusdorf A., Des Forêts G. P., 2023, A&A, 675, A86
Labiano A. et al., 2021, A&A, 656, A57
Lin M.-Y. et al., 2018, MNRAS, 473, 4582
Martín-Navarro I., Pillepich A., Nelson D., Rodriguez-Gomez V., Donnari M., Hernquist L., Springel V., 2021, Nature, 594, 187
Morris S., Ward M., Whittle M., Wilson A., Taylor K., 1985, MNRAS, 216, 193
Mukherjee D., Bicknell G. V., Sutherland R., Wagner A., 2016, MNRAS, 461, 967
Mukherjee D., Bicknell G. V., Wagner A. Y., Sutherland R. S., Silk J., 2018, MNRAS, 479, 5544
Orienti M., Prieto M., 2010, MNRAS, 401, 2599
Pereira-Santaella M., Diamond-Stanic A. M., Alonso-Herrero A., Rieke G. H., 2010, ApJ, 725, 2270
Pereira-Santaella M., Spinoglio L., van der Werf P. P., López J. P., 2014, A&A, 566, A49
Pereira-Santaella M. et al., 2022, A&A, 665, L11
Pereira-Santaella M. et al., 2024, A&A, 685, L13
Perrin M. D., Sivaramakrishnan A., Lajoie C.-P., Elliott E., Pueyo L., Ravindranath S., Albert L., 2014, in Oschmann J. M. Jr, Clampin M., Fazio G. G., MacEwen H. A., eds, SPIE Conf. Ser. Vol. 9143, Space Telescopes and Instrumentation 2014: Optical, Infrared, and Millimeter Wave. SPIE, Bellingham, p. 91433X
Piotrowska J. M., Bluck A. F., Maiolino R., Peng Y., 2022, MNRAS, 512, 1052

[4] https://mast.stsci.edu/portal/Mashup/Clients/Mast/Portal.html

Pound M. W., Wolfire M. G., 2022, AJ, 165, 25
Ramos Almeida C. et al., 2025, A&A, 698, A194
Reunanen J., Prieto M., Siebenmorgen R., 2010, MNRAS, 402, 879
Ricci T., Steiner J. E., May D., Garcia-Rissmann A., Menezes R., 2018, MNRAS, 473, 5334
Riffel R. A., Storchi-Bergmann T., Dors Jr O. L., Winge C., 2009, MNRAS, 393, 783
Riffel R. A. et al., 2016, MNRAS, 461, 4192
Riffel R. A. et al., 2021, MNRAS, 504, 3265
Riffel R. A., Souza-Oliveira G. L., Costa-Souza J. H., Zakamska N. L., Storchi-Bergmann T., Riffel R., Bianchin M., 2025, ApJ, 982, 69
Rigby J. et al., 2023, PASP, 135, 048001
Rigopoulou D., Kunze D., Lutz D., Genzel R., Moorwood A., 2002, A&A, 389, 374
Robitaille T., Deil C., Ginsburg A., 2020, Astrophysics Source Code Library, ascl:2011.023, https://www.ascl.net/2011.023
Rodriguez-Ardila A., Pastoriza M. G., Viegas S., Sigut T., Pradhan A. K., 2004, A&A, 425, 457
Rosenberg M., van der Werf P., Israel F., 2013, A&A, 550, A12
Roussel H. et al., 2007, ApJ, 669, 959
Somerville R. S., Davé R., 2015, ARA&A, 53, 51
Sternberg A., Neufeld D. A., 1999, ApJ, 516, 371
Takahashi J., 2001, ApJ, 561, 254
Thornley M. D., Schreiber N. M. F., Lutz D., Genzel R., Spoon H. W., Kunze D., Sternberg A., 2000, ApJ, 539, 641
Togi A., Smith J. D. T., 2016, ApJ, 830, 18
Vivian U. et al., 2022, ApJ, 940, L5
Ward M., Penston M., Blades J., Turtle A., 1980, MNRAS, 193, 563
Wells M. et al., 2015, PASP, 127, 646
Werner M. W. et al., 2004, ApJS, 154, 1
Wold M., Galliano E., 2006, MNRAS: Letters, 369, L47
Wold M., Lacy M., Käufl H., Siebenmorgen R., 2006, A&A, 460, 449
Xue M., Jiang B., Gao J., Liu J., Wang S., Li A., 2016, ApJS, 224, 23

APPENDIX A: SUPPORTING MATERIAL

In order to facilitate reproducibility of our results, Table A1 provides the relative RA and Dec. of the centre of each of our 0.3 arcsec apertures from the nucleus (which was centred on the spaxel with the highest amount of overall flux across the entire NIRSpec data cube).

Table A1 also provides our derived $\tau_{9.8}$ parameter for each region from applying the differential extinction tool, which we used for correcting for the effects of dust extinction on our measured spectra shown in Fig. 2.

A1 Modelling H_2 excitation diagrams

To understand the observed flux of H_2 rotational lines, we begin by considering the Boltzmann equation, which describes the population distribution across molecular energy states in thermodynamic equilibrium. This can be adapted for a power-law distribution of temperatures, giving the column density, N_i, in a given state i in the following form:

$$N_i = \int_{T_l}^{T_u} \frac{g_i e^{-E_i/k_B T}}{Z(T)} m T^{-n} \mathrm{d}T. \tag{A1}$$

Table A1. Relative RA and Dec offsets for each aperture from the nucleus, as well as the derived $\tau_{9.8}$ for each regions after fitting for differential extinction.

Aperture	ΔRA (arcsec)	ΔDec. (arcsec)	$\tau_{9.8}$
Nucleus	0	0	2.67
SF 1	+0.127	–1.30	1.29
SF 2	–0.565	–1.20	1.61
SF 3	+0.642	+0.90	1.23
Cone 1	–0.863	+0.60	2.39
Cone 2	–1.173	–0.40	1.29

This is simply the Boltzmann equation when assuming our power-law temperature distribution, equation (1), as integrating over just the second part within the integral (mT^{-n}) with respect to temperature would give the total column density. Here g_i is the statistical weight of state, E_i is the energy of the state, k_B is the Boltzmann constant, T is the excitation temperature, and $Z(T)$ is the partition function; a temperature dependent sum over all possible states:

$$Z(T) = \sum_i g_i e^{-E_i/k_B T}. \tag{A2}$$

The relative population of these states is determined by the exponential term, meaning that higher energy states become increasingly populated as the temperature rises. The observed flux of a given rotational line is directly proportional to the column density in the corresponding upper energy state. For an optically thin transition between levels $J+2 \rightarrow J$, the observed flux can then be expressed as:

$$F_J = \frac{h\nu A_J N_{J+2} \Omega}{4\pi}, \tag{A3}$$

where h is Planck's constant, ν is the frequency of the transition, A_J is the Einstein spontaneous transition rate, and Ω is the solid angle of the aperture. Here, the column density N_{J+2} represents the population in the upper state of the transition.

To construct the H_2 excitation diagram, we plot the inferred column density for each state, N_{J+2}, normalized by its statistical weight, g_{J+2}. Assuming a fixed ortho-to-para ratio of 3:1 simplifies the statistical weights to $g_J = 2J+1$ for even (para-) H_2 and $g_J = 3(2J+1)$ for odd (ortho-) H_2.

By plotting these column densities logarithmically (we use $\log_{10}$ here) against the upper state energy divided by Boltzmann's constant, E_u/k_B, we obtain the excitation diagram. This representation allows the excitation temperature to be inferred from the slope of the data points. While the upper state energy often exceeds the actual gas temperature [e.g. $E_u/k_B \sim 1050$ K for the S(1) transition], recall that significant emission can still arise from cooler regions (e.g. down to $T \sim 150$ K).

We also provide the excitation diagrams for every region plotted separately in Fig. A1, as opposed to Fig. 5 in which every region was plotted together for each model. Plotting based on region instead (as in Fig. A1) allows for easier comparison between models for each region.

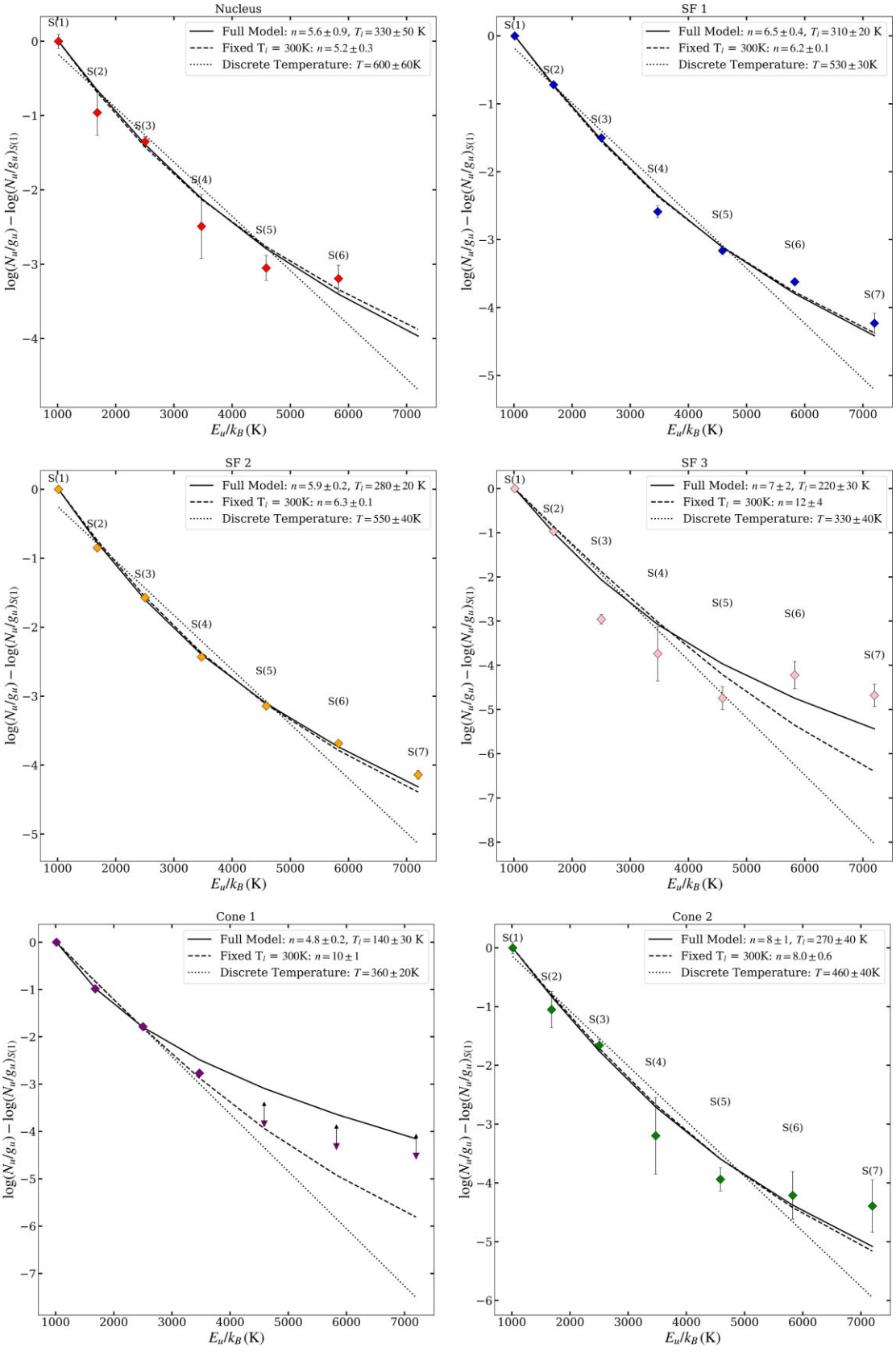

Figure A1. Excitation diagram fits shown for each aperture separately.

[1]*Department of Physics, University of Oxford, Keble Road, Oxford OX1 3RH, UK*
[2]*School of Sciences, European University Cyprus, Diogenes street, Engomi, 1516 Nicosia, Cyprus*
[3]*Centro de Astrobiología (CAB), CSIC-INTA, Camino Bajo del 497 Castillo s/n, E-28692 Villanueva de la Cañada, Madrid, Spain*
[4]*Instituto de Astrofísica de Canarias, Calle Vía Láctea, s/n, E-38205 La Laguna, Tenerife, Spain*
[5]*Departamento de Astrofísica, Universidad de La Laguna, E-28206 La Laguna, Tenerife, Spain*
[6]*Departmento de Física de la Tierra y Astrofísica, Fac. de CC Físicas, Universidad Complutense de Madrid, E-28040 Madrid, Spain*
[7]*School of Mathematics, Statistics and Physics, Newcastle University, Newcastle upon Tyne NE1 7RU, UK*
[8]*Observatoire de Paris, LUX, Collège de France, CNRS, PSL University, Sorbonne University, F-75014 Paris, France*
[9]*Max Planck Institute for extraterrestrial Physics, Giessenbachstrasse 1, D-85748 Garching, Germany*
[10]*Department of Physics & Astronomy, University of Alaska Anchorage, Anchorage, AK 99508-4664, USA*
[11]*Department of Physics, University of Alaska Fairbanks, Fairbanks, AK 99775-5920, USA*
[12]*Observatorio Astronómico Nacional (OAN-IGN)-Observatorio de Madrid, Alfonso XII, 3, E-28014 Madrid, Spain*
[13]*Instituto de Radioastrononomía y Astrofí sica (IRyA), Universidad Nacional Autonoma de Mexico, Antigua Carretera a Pátzcuaro #8701, Ex-Hda. San José de la Huerta, C.P. 58089, Morelia, Michoacán, Mexico*
[14]*Department of Physics and Astronomy, The University of Texas at San Antonio, 1 UTSA Circle, San Antonio, TX 78249, USA*
[15]*School of Physics and Astronomy, University of Southampton, Southampton SO17 1BJ, UK*
[16]*Space Telescope Science Institute, San Martin Drive, Baltimore, MD 21218, USA*
[17]*National Astronomical Observatory of Japan, National Institutes of Natural Sciences (NINS), 2-21-1 Osawa, Mitaka, Tokyo 181-8588, Japan*
[18]*Instituto de Física Fundamental, CSIC, Calle Serrano 123, E-28006 Madrid, Spain*
[19]*Department of Astronomy, University of Geneva, ch. d'Ecogia 16, CH-1290 Versoix, Switzerland*
[20]*Instituto de Estudios Astrofísicos, Facultad de Ingeniería y Ciencias, Universidad Diego Portales, Av. Ejército Libertador 441, Santiago, Chile*
[21]*Departamento de Física, CCNE, Universidade Federal de Santa Maria, 97105-900 Santa Maria, RS, Brazil*
[22]*Centro de Astrobiología (CAB), CSIC-INTA, Ctra. de Ajalvir km 4, Torrejón de Ardoz, E-28850 Madrid, Spain*

This paper has been typeset from a TEX/LATEX file prepared by the author.